THEORY DRIVEN DESIGN OF FUNCTIONAL MATERIALS AT INTERFACES

A Thesis

Presented to the Faculty of the Graduate School

of Cornell University

in Partial Fulfillment of the Requirements for the Degree of

Master of Science

by

Akif Yalcin Ozhabes

January 2017

ABSTRACT

First principle calculations and computational chemistry not only benefits from the advancements in computer technologies but also from the improvements in the theory itself to enhance performance. For example, recently developed Joint Density-Functional Theory (JDFT) provides us with the tools to study solvated systems efficiently, removing the need for sampling the phase space of the fluid. It enables the calculation of thermodynamic averages with little computational overhead and without sacrificing the rigor of *ab initio* physics. This thesis starts with a brief summary of the theory that sets the basis of electronic structure calculations. We follow by the application targeting two physical systems of technological importance: Rechargeable batteries in the context of preventing dendritic growth upon charging and Nb_3Sn superconducting radio frequency cavities focusing on the microscopic mechanisms by which niobium transforms into niobium-tin during the coating process. For the first, we develop a macroscopic model to analyze the stability of a surface growing via electrodeposition (a charging battery electrode fits this description) and we calculate material specific parameters that appear in the model for various compounds found in battery systems. For the second, we present various defect energies and two possible transformation pathways from body-centered cubic structure (niobium bulk) to A15 structure (niobium-tin). We continue with a proof of concept and describe why combining molecular dynamics with Joint Density-Functional Theory should reproduce the correct rates of rare events. As a test system, we choose OH^- moving in water via proton hopping (Grotthuss mechanism) and our initial results show that JDFT dynamics is a promising new way to estimate

rare event rates in fluid environments.

BIOGRAPHICAL SKETCH

Yalcin Ozhabes was born in Istanbul, Turkey, in 1989. He attended Galatasaray High School (Lycée de Galatasaray) then studied physics and mechanical engineering at Bogazici University in Istanbul as an undergraduate student where he conducted research under the guidance of Professor Muhittin Mungan. Since August 2013, he has been a graduate student in Cornell University Physics department. Under the supervision of Professor Tomás Arias, he has been a research assistant working in computational physics. Upon completion of his Master's degree in physics, he plans to pursue a career in software engineering.

This document is dedicated to the scientific community.

ACKNOWLEDGEMENTS

It was a great pleasure to work with my advisor Tomás Arias. He is extremely brilliant not only as a theoretical physicist, but also as an influential communicator. The way he presents his ideas to the outside world and the way he communicates with his students both as an advisor and as a teacher is highly positive and inspiring. I am very grateful to him for keeping me excited and motivated when my results were discouraging, for letting me chase my passions outside the field and for being a person that I can always look up to.

Deniz Gunceler, being the only other Turkish group member, was more like an older brother to me. He was a great mentor and a hard working colleague who pushed me only forward. I am thankful for his selfless efforts to help me and appreciative of his lifelong friendship. I am also grateful to the former members of our group, Kendra Letchworth-Weaver, Ravishankar Sundararaman, and Christine Umbright for their guidance. Furthermore, I owe thanks to Michelle Kelley and to the new members of our group, Nathan Sitaraman, Kevin Nangoi and Victoria Litvinova for the fruitful discussions and for helping me to write this thesis. It makes me sad that I am missing all the color and joy you will be bringing to the office.

I would like to thank the other members of my special committee, Matthias Liepe for organizing and running the Center for Bright Beams meetings facilitating collaboration and Erich Mueller for being an inspiring teacher.

I am thankful to my partner, Ecem Ozinan for her love and support. I strongly appreciate the encouragement and the help of my parents, my sister Pinar Ozhabes and my brother Efe Yigitbasi which has made this adventure possible.

Ithaca has been my home for four years and its infamous cold has made me

only warmer with all the friendships it has offered. Salvator Lombardo, Hao Shi, Ran Wei, Katherine Quinn and many others have always been one phone call away. I have made great friends in the Turkish community in Ithaca. I would like to thank Murat Uralkan, Zeyneb Saraoglu, Mehmet Demirtas, Melik Turker, Can Bilir, Hakan Atakisi, Efe Gencer, Baris Bircan for their friendship and Anil Akturk and Elif Korkmaz for both their friendship and for their service as the president of the Cornell Turkish Student Association.

I am also thankful to the entire Physics Department at Cornell University as they deliver on their promise to make the graduate life more cooperative than competitive.

TABLE OF CONTENTS

LIST OF TABLES

LIST OF FIGURES

CHAPTER 1

INTRODUCTION

1.1 From the first principles

One thing that separates humans from all the other living creatures is our ability to shape the world around us. We achieve this by the means of science which allows us to understand how nature works. But what exactly is *understanding*? To me, it is finding the connections between seemingly unrelated events. For example, when Isaac Newton described the free falling of an apple and the rising and setting of the sun in the sky as the logical consequence of the same set of definitions, that was a big leap in *"understanding"*.

With quantum mechanics, we also made lots of connections between intuitively disconnected physical phenomena. An idea once proposed to describe the physics of small length scales, was able to bridge the gap to macroscopic scale by reproducing Newton's description. From the diffraction patterns of light to the mechanical properties of materials, all were connected with the same set of equations, the equations of quantum mechanics. Even though famous physicist Richard Feynman claimed that nobody truly understands quantum mechanics, the application of the theory is so broad and successful that it certainly is another big leap forward in our understanding of the universe.

Today, we are able to understand the physics of materials starting from the atomic scale, applying the laws of electromagnetism and non-relativistic quantum mechanics. Relativistic effects may become important for heavier atoms but for the first four rows of the periodic table, which covers 99% of terrestrial

materials, they are negligible. Schrödinger's formulation of quantum mechanics, in its time-independent form reads

$$\hat{H}\Psi = E\Psi \tag{1.1}$$

The Hamiltonian ($\hat{H}$) of interest describing the physics of atoms is the spin-independent many body Hamiltonian for electrons and nuclei:

$$\hat{H} = -\frac{1}{2}\sum_i \boldsymbol{\nabla}_i^2 + \sum_{i<j}\frac{1}{\left|\vec{r_i} - \vec{r_j}\right|} - \sum_{i,\alpha}\frac{Z_\alpha}{\left|\vec{r_i} - \vec{R_\alpha}\right|} - \sum_\alpha \frac{1}{2M_\alpha}\boldsymbol{\nabla}_\alpha^2 + \sum_{\alpha<\beta}\frac{Z_\alpha Z_\beta}{\left|\vec{R_\alpha} - \vec{R_\beta}\right|} \tag{1.2}$$

The latin letter indices are reserved for electrons and the greek letters runs over the nuclei. M_α's are the mass of the respective nuclei and Z_α is its charge. $\vec{R_\alpha}$ and $\vec{r_i}$ are the coordinates for the nuclei and electrons respectively. Solving Eq. 1.1 for the many body wave function $\Psi(\{\vec{r_i}\}, \{\vec{R_\alpha}\})$ with the appropriate antisymmetric behavior under the interchange of two electronic coordinates gives the energy levels E of the system. Particularly the lowest energy state, the ground state, is the most tenable one given the characteristic energies encountered in chemistry.

Another assumption we can make is the Born-Oppenheimer approximation which allows us to treat the nuclei classically rather than quantum mechanically [11]. We can treat the nuclei as point particles and the many body wavefunction is reduced to have only the electronic degrees of freedom. After this separation, we are left with the electronic Hamiltonian in which the effect of nuclei is treated as an external potential $V_{\text{ext}}(\vec{r})$.

$$V_{\text{ext}}(\vec{r}) = \sum_\alpha \frac{Z_\alpha}{\left|\vec{r} - \vec{R_\alpha}\right|} \tag{1.3}$$

The Schrödinger's equation after Born-Oppenheimer approximation be-

comes

$$\left(-\frac{1}{2}\sum_i \boldsymbol{\nabla}_i^2 + \sum_{i<j}\frac{1}{\left|\vec{r_i}-\vec{r_j}\right|} - \sum_i V_{\text{ext}}(\vec{r_i})\right)\Psi(\vec{r_1},\vec{r_2},...,\vec{r_N}) = E_{\text{el}}\Psi(\vec{r_1},\vec{r_2},...,\vec{r_N}) \tag{1.4}$$

and the total energy of the system also includes the energy of the nuclei:

$$E_{\text{tot}} = E_{\text{el}} + U_{\text{nuc}} + E_{\text{Kin-nuc}} \tag{1.5}$$

where U_{nuc} is the electrostatic potential energy that comes from the nuclei-nuclei repulsion (last term of Eq. 1.2) and $E_{\text{Kin-nuc}}$ is the classical kinetic energy of the nuclei.

1.2 Density Functional Theory

Eq. 1.4 is very powerful but exact solutions are attainable only for the simplest systems. When attacked computationally, the representation of $\Psi(\{\vec{r_i}\})$ grows exponentially with the number of electrons, making it impossible to solve for large systems with many electrons. That is why nowadays approximating the solution to Eq. 1.4 for better computational scaling is a huge field of research.

In order to motivate the approximation schemes, let us rewrite the energy terms derived from the many-body Schrödinger equation in terms of density matrices.

$$\begin{aligned}\hat{H} &= \hat{T} + \hat{W}_{\text{el-el}} + \hat{V}_{\text{ext}} \\ &= -\frac{1}{2}\sum_i \boldsymbol{\nabla}_i^2 + \sum_{i<j}\frac{1}{\left|\vec{r_i}-\vec{r_j}\right|} - \sum_i V_{\text{ext}}(\vec{r_i})\end{aligned} \tag{1.6}$$

$$\begin{aligned}\langle \hat{H} \rangle &= \langle \Psi | \hat{H} | \Psi \rangle \\ &= \langle \Psi | \hat{T} | \Psi \rangle + \langle \Psi | \hat{W}_{\text{el-el}} | \Psi \rangle + \langle \Psi | \hat{V}_{\text{ext}} | \Psi \rangle \\ &= E_{\text{Kin}} + E_{\text{int}} + E_{\text{pot}}\end{aligned} \tag{1.7}$$

The kinetic energy term and the external potential energy term are single particle interactions and for an arbitrary single particle operator $\hat{T} = \sum_i \hat{t}(\vec{r}_i)$, the expectation value can be written in terms of the single particle density matrix ρ_1 as

$$\langle \hat{T} \rangle = \int d^3 r \left[\hat{t}(\vec{r}) \, \rho_1(\vec{r}, \vec{r}') \right]_{\vec{r}'=\vec{r}} . \tag{1.8}$$

The electron-electron Coulombic interaction term requires the two particle density matrix. For a symmetric interaction kernel $\hat{w}(\vec{r_1}, \vec{r_2})$ which gives the many body interaction operator by $\hat{W} = \sum_{i \neq j} \hat{w}(\vec{r_i}, \vec{r_j})$

$$\langle \hat{W} \rangle = \int d^3 r_1 d^3 r_2 \left[\hat{w}(\vec{r_1}, \vec{r_2}) \, \rho_2(\vec{r_1}, \vec{r_2}; \vec{r_1}', \vec{r_2}') \right]_{\vec{r_1}'=\vec{r_1},\ \vec{r_2}'=\vec{r_2}} \tag{1.9}$$

The single (ρ_1) and two particle (ρ_2) density matrices are given by:

$$\rho_1(\vec{r}, \vec{r}') = N \int d^3 r_2 d^3 r_3 ... d^3 r_N \; \Psi^*(\vec{r}, \vec{r_2}, ..., \vec{r_N}) \; \Psi(\vec{r}', \vec{r_2}, ..., \vec{r_N}) \tag{1.10}$$

$$\rho_2(\vec{r_1}, \vec{r_2}; \vec{r_1}', \vec{r_2}') = \frac{N(N-1)}{2} \int d^3 r_3 ... d^3 r_N \; \Psi^*(\vec{r_1}, \vec{r_2}, \vec{r_3}, ..., \vec{r_N}) \; \Psi(\vec{r_1}', \vec{r_2}', \vec{r_3}, ..., \vec{r_N}) \tag{1.11}$$

There is one more simplification we can make when the kernel of the operators commutes with the position operator (which is the case for the external potential or the Coulomb kernel for electron electron interaction $^1/_2 \left| \vec{r}_i - \vec{r}_j \right|^{-1}$). We can express the expected values of these operators in terms of density functions: for the external potential, it is the electron density $n(\vec{r}) = \rho_1(\vec{r}, \vec{r})$ and for the electron-electron repulsion energy it is the pair density function

$n_2(\vec{r},\vec{r}') = \rho_2(\vec{r},\vec{r}';\vec{r},\vec{r}')$:

$$\begin{aligned} \langle \hat{V}_{\text{ext}} \rangle &= \int d^3r\, v(\vec{r})\, \rho_1(\vec{r},\vec{r}) \\ \langle \hat{W} \rangle &= \int d^3r\, d^3r'\, w(\vec{r},\vec{r}')\, \rho_2(\vec{r},\vec{r}';\vec{r},\vec{r}')\ . \end{aligned} \tag{1.12}$$

In this notation, it is not hard to write the energy as:

$$\begin{aligned} E_{\text{el}} = &-\frac{1}{2}\int d^3r\, \left[\nabla^2 \rho_1(\vec{r},\vec{r}')\right]_{\vec{r}'=\vec{r}} \\ &+ \int d^3r\, v(\vec{r})\, n(\vec{r}) \\ &+ \frac{1}{2}\int d^3r\, d^3r'\, n(\vec{r}) \frac{1}{\left|\vec{r}-\vec{r}'\right|}\, n(\vec{r}') \\ &+ \frac{1}{2}\int d^3r\, d^3r' \frac{1}{\left|\vec{r}-\vec{r}'\right|}\Big[n_2(\vec{r},\vec{r}') - n(\vec{r})n(\vec{r}')\Big] \\ = &\, E_{\text{Kin}} + E_{\text{pot}} + E_{\text{H}} + U_{\text{XC}} \end{aligned} \tag{1.13}$$

The expression above is still too difficult to evaluate for a real system. The earliest approximation method was independently developed by Llewellyn Thomas and Enrico Fermi. The so called Thomas-Fermi approximation rewrites the energy in terms of electron density $n(\vec{r})$ only. They ignored the exchange-correlation term (U_{XC}) and approximated the kinetic energy term assuming non-interacting homogeneous electron gas. Being a very crude approximation, it does not give any predictive power yet has a conceptual importance as it is exact in certain limits. [21, 57, 95]

Hartree-Fock theory is based on the assumption that the many body wave-function can be formed as a single Slater determinant. This assumption is more successful in estimating molecular behavior with electrons localized in orbitals. However, a single Slater determinant ignores electronic correlation. Increasing the accuracy is possible with post Hartree-Fock methods. Møller-Plesset method deals with the Coulombic correlations perturbatively. Configuration

integration and coupled cluster techniques represent the many body wavefunction as a linear combination of multiple Slater determinants [22].

The formal definition of density functional theory originates from the Hohenberg-Kohn theorems.[39] In their nominal work, they show that there is a one-to-one mapping between the ground state electron density $n_0(\vec{r})$ and the external potential $V_{\text{ext}}(\vec{r})$. With this formal definition, the electronic ground state energy can be written as the minimum of the energy functional

$$E_{\text{el}} = \min_{n(\vec{r})} \left\{ F_{\text{HK}}[n(\vec{r})] + \int d^3r \; V_{\text{ext}}(\vec{r}) \; n(\vec{r}) \right\} \tag{1.14}$$

The universal functional F_{HK} is a definition following a proof of existence. In other words, we do not have a machinery to evaluate F_{HK} exactly, we only know its existence and it is yet to be approximated. Even more problematic, within the limits of Hohenberg-Kohn theory, the minimization is not over all possible $n(\vec{r})$'s but only over the densities that yield to a ground state[1]. However, at this point Thomas-Fermi theory can be seen as one way to approximate the universal Hohenberg-Kohn functional.

To tackle with the shortcomings of Thomas-Fermi approximation, Kohn and Sham proposed a better way to calculate the kinetic energy, given a density $n(\vec{r})$. They formulated the kinetic energy as if the density $n(\vec{r})$ comes from the ground state of a non-interacting electronic system in an effective potential.

$$T_{\text{KS}}\left[n(\vec{r})\right] = \min_{\phi_i} \left\{ \sum_i -\frac{1}{2} \langle \phi_i | \nabla^2 | \phi_i \rangle \,\middle|\, \{\phi_i\} \text{ orthonormal and yielding to } n(\vec{r}) \right\} \tag{1.15}$$

Given this definition for kinetic energy, they also define the exchange-correlation energy as the remaining part of the Hohenberg-Kohn functional:

$$E_{\text{XC}}[n(\vec{r})] = F_{\text{HK}}[n(\vec{r})] - T_{\text{KS}}[n(\vec{r})] - E_{\text{pot}}[n(\vec{r})] - E_{\text{H}}[n(\vec{r})] \tag{1.16}$$

[1]This is known as v-representability problem and 15 years after the development of Hohenberg-Kohn theorem, Levy and Lieb showed how this can be avoided [55, 56].

This decomposition yields the Kohn-Sham equations, single particle time independent Schrödinger equation in a modified potential:

$$\left(-\frac{\nabla^2}{2} + V_{\text{ext}} + V_{\text{H}} + V_{\text{XC}}\right)\phi = \epsilon\phi \tag{1.17}$$

The exchange-correlation potential (V_{XC}) does not have an explicit form. However, having the kinetic energy more accurately described, estimating V_{XC} using the local density approximation (LDA) which assumes the homogeneous electron gas works well reproducing the experimental measurements to great accuracy. The generalized gradient approximation (GGA) uses the local gradient of the density in addition to the local value of the density. There are many flavors of exchange correlation functionals that one can pick depending on the physics they want to capture and computational accuracy they want to attain.

1.3 Joint Density Functional Theory

Joint density functional theory (JDFT) is the framework to study electronic systems in contact with a fluid environment. The main motivation behind the development of the theory historically has been to study electrochemical systems. Nevertheless, the methods are in principle exact for any solvated system, such as biological molecules.

JDFT combines the classical density functional theory of liquids with the electronic density functional theory. Classical density functional theory follows an approach similar to Hohenberg-Kohn theorems.[32] The quantum mechanically described grand free energy of the fluid system is rewritten in terms of the

site densities. In terms of density matrix (P), the equilibrium free energy for the fluid is:

$$\Phi_0 = \min_P \left[\mathrm{Tr}(\hat{H}P + TP\ln P) + \sum_a \int d^3r (V_a(\vec{r}) - \mu_a) N_a(\vec{r}) \right] \tag{1.18}$$

where $N_a(\vec{r})$ is the nuclear density of species a that correspond to the density matrix P. The re-expression of the minimization yields:

$$\begin{aligned} \Phi_0 &= \min_{\{N_a\}} \left[\min_{P\to\{N_a\}} \mathrm{Tr}(\hat{H}P + TP\ln P) + \sum_a \int d^3r (V_a(\vec{r}) - \mu_a) N_a(\vec{r}) \right] \\ &\equiv \min_{\{N_a\}} \left[\Phi_{\mathrm{CDFT}}[\{N_a\}] + \sum_a \int d^3r (V_a(\vec{r}) - \mu_a) N_a(\vec{r}) \right] \end{aligned} \tag{1.19}$$

Φ_{CDFT} is, just like F_{HK}, an in principle exact functional, but practically needs approximations. It is proven possible to extend the same formalism to describe the solute-solvent systems after partitioning the electron density of the combined system into solute and fluid contributions. Then the fluid contributions to the electron density are integrated out.[78]

$$\Phi_0 = \min_{\{n,N_a\}} \left[\Phi_{\mathrm{JDFT}}[n,\{N_a\}] + \int d^3r\, V_{\mathrm{ext}}(\vec{r})\, n(\vec{r}) + \sum_a \int d^3r (V_a(\vec{r}) - \mu_a) N_a(\vec{r}) \right] \tag{1.20}$$

The minimization in Eq. 1.20 runs over solute electron density n, and the fluid site densities N_a. It is common to approximate Φ_{JDFT} after separating the known contributions as:

$$\Phi_{\mathrm{JDFT}}[n,\{N_a\}] = F_{\mathrm{HK}}[n] + \Phi_{\mathrm{CDFT}}[\{N_a\}] + \Delta\Phi[n,\{N_a\}] \tag{1.21}$$

where $\Delta\Phi[n,\{N_a\}]$ is the coupling term between the electronic density and the site densities and it is formally defined as the difference between the exact JDFT free energy functional and the sum of Hohenberg-Kohn functional and classical density functional of liquids. The approximation schemes of the coupling term is an active research area and it is the key to the success of Joint density functional theory.[53]

Polarizable continuum models (PCMs) form a class of highly simplified low cost models. In these methods, the solvent environment is approximated by a dielectric field. There are further corrections for the formation energy of the cavity that the solute resides in and for dispersion energies. In this thesis, we use the nonlinear PCM to model the fluid effects, which is further explained in chapter 2.

1.4 Plan

The tools of computational chemistry, briefly summarized in this chapter, allow us to study various systems. Following the first principles approach, we can attack the problems at the microscopic level resolving the atoms and electrons. In chapter 2, we study battery systems and search for possible mechanisms to mitigate the main problem of next generation of rechargeable batteries, namely the dendritic growth. We prove that JDFT can provide guidance for experimental studies, allowing rapid technological advancement. In chapter 3, we study the microscopic properties of niobium-tin system, which is considered as the successor of niobium superconductors in accelerator technologies. In chapter 4, we introduce JDFT dynamics as a computationally efficient way of simulating rare event dynamics.

CHAPTER 2

STABILITY OF GROWING SURFACES UNDER ELECTRODEPOSITION IN METAL ANODE BATTERIES

Parts of this chapter also appeared in the dissertation written by Deniz Gunceler. It is taken from the same manuscript which I am the co-author of.

Development of more efficient energy storage technologies is needed to build a more sustainable future. Understanding physical processes at the atomic scale on electrode-electrolyte interfaces is an important intermediate step towards realizing this goal. Motivated by the desire to help enable many new applications, ranging from grid storage to long-ranged electric cars, researchers have also been using the tools of *ab initio* electronic structure to help develop better rechargeable batteries. [14, 25, 30, 31, 38, 40, 41, 46, 54, 67, 69, 76, 77, 85–87, 92, 94]

The current state-of-the-art in rechargeable batteries is lithium-ion technology, where the presence of a graphitic anode host results in deadweight (carbon) to be carried along with the battery. Metallic anodes would be a better choice due to their increased energy density ($\sim$ 3860 $mAhg^{-1}$), [73, 106] but they suffer from localized nucleation while charging and form needle-like structures called *dendrites*. [27, 68, 73] Despite many years of concentrated effort, there are still many unanswered questions about the underlying physical mechanisms of dendrite initiation and growth. This is partly due to the complex nature of the passivation layer, also called the solid-electrolyte interface (SEI), that forms when the metallic electrode comes in contact with the electrolyte. [19, 74, 88] Existing ideas and models on dendritic electrodeposition of lithium suggest that chemical inhomogeneities in the SEI layer result in spatially varying rates of deposition on the surface, which then lead to instabilities because any protrusion

tends to concentrate electric field lines. [15, 16, 33, 63, 79, 82, 96]

Recent experiments have shown that the composition of the SEI layer has a dramatic effect on the performance of the battery cell. Based on our previous theoretical work, [30, 31] Tu et. al. have managed to suppress dendrite growth in liquid and nanoporous electrolytes by passivating the surface of the anode with lithium-halides. [58] Likewise, researchers from Stanford have succeeded in designing an interfacial layer from carbon nanospheres which improves cycling efficiency. [106] Understandably, these results and many others stimulate a strong interest in studying the fundamental physical mechanisms within the SEI layer, and to date, many studies have investigated the bulk properties of these materials (e.g. bulk diffusion of Lithium). [85–87]

The rich physics at the interface between anode and liquid electrolyte is much less understood, though there have been very promising new developments in this field as well. [24, 31, 40, 106] Very recently, Jäckle and Groß have published a comparative study of metallic Lithium, Sodium and Magnesium surfaces. [40] Their DFT calculations suggest that surface diffusion is significantly faster on magnesium metal than on lithium metal, which may be important to understand why lithium forms dendrites while magnesium does not. While this work is very important, we believe (and the authors themselves also point out) that more investigation in this area is needed because that work does not address the presence and the effect of the electrolyte and, critically, the fact that metallic electrodes do not present pure surfaces to the electrolyte but rather complex non-metallic passivating layers known as SEI.

In this chapter, we focus on the physical processes on the surfaces of various SEI materials for metallic anodes. In particular, we provide an explanation of

the physical mechanisms by which halogen additives (especially bromine) to the electrolyte suppress the irregularities on the surface and improve cycling efficiency [45, 51, 58–60, 64]. To this end, we utilize density functional theory to calculate surface cleavage energies and surface diffusion barriers for the most commonly reported SEI materials in the literature, [6, 8, 105] and then use these results to help understand the experimentally observed trends. Our hope is that such understanding will accelerate the development of novel anode materials to improve battery performance. Our results support the growing belief [30, 31, 40, 58, 96] that anode materials with high surface energy and surface mobility are desirable. We also detail our previous claim, [31] recently supported by experiment, [58] that Lithium-halide SEI layers have these desirable properties and that they are effective in suppressing dendrite growth on metallic lithium anodes.

2.1 Computational Methods

To perform first principles DFT calculations, we use the open source JDFTx software[89] which is based on the direct minimization of an analytically continued total energy functional. [4] Ultra-soft pseudopotentials [102] from the GBRV library[26] are generated using the Vanderbilt pseudopotential code. [1] To account for electronic exchange and correlation, we use the PBE flavor of the generalized gradient approximation. [75] Throughout this methods section, we work in standard atomic units; i.e. bohr (a_0) for distances and hartree (E_h) for energies. All results in the sections below will be presented in more familiar SI units.

For the Brillouin zone sampling of bulk units, we use a k-point grid of 4×4×4

which we determined by converging the total energy to a level of $10^{-4}\ E_\mathrm{h}$. The energy cut-off for the plane wave basis was $20\ E_\mathrm{h}$ which was also consistent with the same convergence threshold. The nuclei were relaxed until the root mean square of the forces were below $10^{-4}\ E_\mathrm{h}/a_0$.

To test our choice pseudopotentials as well as other calculation parameters, we calculated lattice constants of various lithium and sodium SEI materials. The results, plotted in figure 2.1, were satisfactory. (It is our belief that DFT has the largest error in the lattice constant of LiOH because LiOH has a layered structure where long-ranged dispersion interactions play an important role.)

To calculate the surface formation energies, we create slabs varying in size from compound to compound. To determine the thickness of each slab, we take the number of layers that are necessary to converge the surface energy to a level of $10^{-4}\ E_\mathrm{h}$ per unit cell. The vacuum layer (or solvent for fluid calculations) between the slabs is $20\,a_0$, allowing us to collapse the three dimensional k-point grid to a planar grid. The center layer is held fixed and the rest of the slab is relaxed with the same convergence criteria mentioned for the bulk calculations. Where needed, we use a truncated Coulomb kernel [90] along the slab axis to prevent spurious electrostatic interactions between slabs. Then we calculate surface formation energies by taking the difference of the slab energy and the energy of equal number of formula units in the bulk and then dividing by the surface area.

$$E_\mathrm{surf} = \frac{1}{2A}(E_\mathrm{slab} - E_\mathrm{bulk}) \tag{2.1}$$

For all crystals, we pick the surface with the lowest surface energy. (100 for halides, 001 for LiOH and Li_2CO_3, 111 for Li_2O)

To study surface diffusion, we consider the hopping process of an adatom

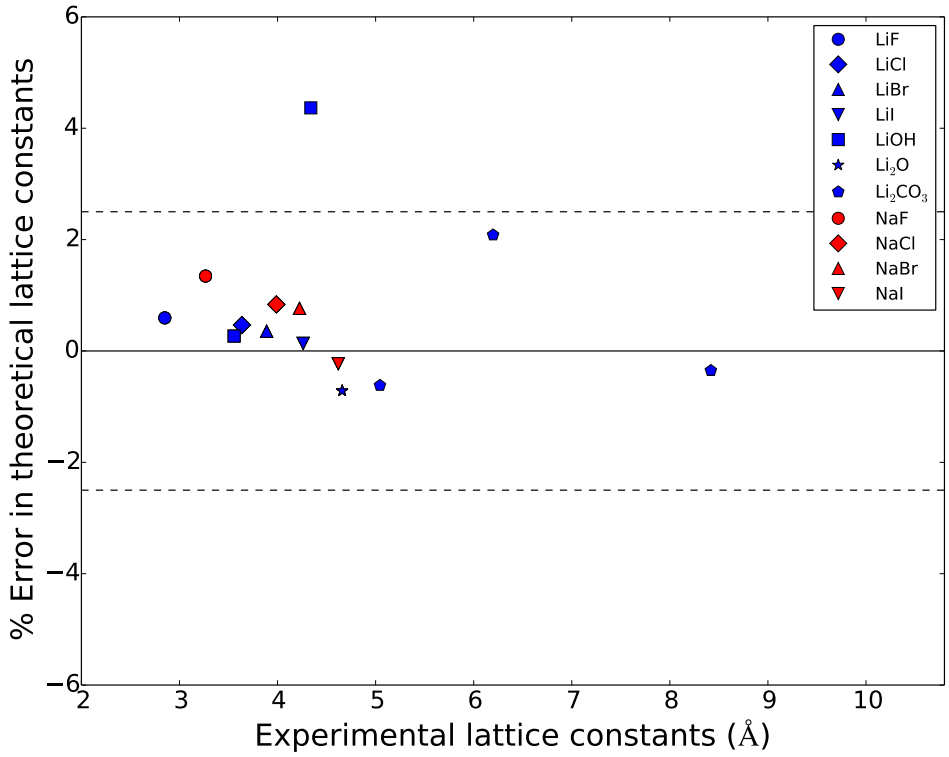

Figure 2.1: The percentage error in DFT lattice constants, plotted as a function of the experimental lattice constants. The solid black line represents exact agreement of theory and experiment. The dashed black lines represent ±2.5% deviations from experiment.

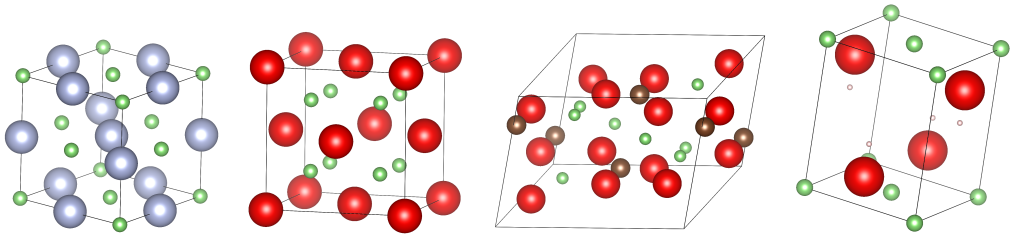

Figure 2.2: From left to right: rocksalt (halides), anti-fluorite (Li_2O), zabuyelite (Li_2CO_3) and LiOH. Pictures were made using VESTA. [66]

that moves from one equilibrium position to the other and whose rate depends on the energy barrier along that path. We determine the diffusion path by comparing the binding energies of the adatom at the high symmetry points along the surface, letting the adatom relax in the direction parallel to the slab normal. Once we determine the endpoints of the diffusion pathway, we carry out a series of intermediate calculations by putting the adatom in a series of sites equally spaced on the line connecting the two binding sites. For these calculations, the entire slab relaxes except the middle layer, while the adatoms are restricted to stay on the plane perpendicular to the diffusion path. To minimize the interactions between periodic images of adatoms, we use 3×3 supercells.

Standard plane-wave electronic structure methods have difficulty handling interfaces between battery electrodes and the electrolyte, [84] largely due to the need to thermodynamically sample the configuration space of the liquid electrolyte. As a result, there have been fewer *ab inito* investigations of lithium metal anode-electrolyte interfaces compared to, for example, the investigations of the bulk properties of lithium intercalation compounds. [25, 38, 76, 77, 92, 94]

In principle, one can sample the configuration space of the electrolyte using *ab initio* molecular dynamics, [24, 54] and further accelerate the calculation using hybrid techniques such as QM/MM. [44] However, calculation of free energies with these methods are difficult and these approaches often do not easily scale to the large number of materials we want to study. An alternative approach is that of continuum solvation models, [3, 29, 30] where the individual molecules in the liquid electrolyte are replaced with a continuum field, and thus free energies can be computed with a single density-functional calculation. Fortunately, recent developments in continuum solvation models [3, 29, 30, 91] have made

it feasible to efficiently study the solid-liquid interfaces for a large number of material/electrolyte combinations.

In this work, we use a nonlinear polarizable continuum model which models the electrolyte environment as a continuous field of interacting dipoles. [30] This approach can also capture dielectric saturation effects, which are important near the surfaces of highly polar materials such as the Lithium SEI surfaces we consider here. In this nonlinear continuum model, the density profile of the electrolyte ($s(\vec{r})$) is computed self-consistently from the electron density of the surface slab ($n(\vec{r})$) as

$$s(\vec{r}) = \text{erfc}\frac{\ln(n(\vec{r})/n_c)}{\sigma\sqrt{2}}, \tag{2.2}$$

where σ (= 0.6) determines the width of the transition region that is set to be resolvable on the FFT grid and n_c is a (solvent-dependent[29]) critical electron density value that determines the location of the solute-solvent interface. For the non-electrostatic terms in the surface-electrolyte interaction, (such as cavitation entropy and long-ranged van der Waals) we make use of the effective surface tension approximation, [3] which modifies the bulk (macroscopic) surface tension of the electrolyte to approximate these contributions.

2.2 Surface energies and diffusion

The formation of dendrites represents an increase in surface area. The thermodynamic perspective would thus indicate that SEI materials with greater surface energies should offer greater dendrite resistance. Furthermore, dendrite nucleation may be driven by cracks in the SEI, [73] so that a stable SEI with a high surface formation energy would offer resistance to this mechanism as well.

However, the kinetics during electrodeposition might very well drive the system far from equilibrium. Therefore, one must also consider the mechanism by which surface energy would tend to suppress dendrites, namely surface diffusion. Following the same train of thought, one expects that materials with fast surface diffusion, for example those with small diffusion barriers for adatoms, would be less likely to form dendrites.

This section is broken into four parts: In the first part, we develop a macroscopic model by which we understand the nucleation of irregularities on a initially flat surface upon electrodeposition. In the second part, we evaluate the results of this model for various SEI materials. In the third part, we summarize our results from the first principle calculations for the surface energies and diffusion barrier heights for many candidate SEI materials, and discuss the trends we observe. Finally, we investigate a binding-site switching mechanism that results in unusually low diffusion barriers for some alkali-halides.

2.2.1 Modeling the surface growth

In order to understand the effect of competing terms that drive the system towards and away from the stable growth, we develop a macroscopic continuum model of the growing surface. We take into account the locally varying deposition rates due to concentrated electric field lines near the irregularities as a source of instability. Additionally, the energy cost of increasing the surface area effectively creates a thermodynamic force that stabilizes the surface.

In our simplified picture (sketched in Figure 2.3), we have metal electrode surface whose shape is $s(x, y; t)$ and on top of it, we have a thin SEI layer, as-

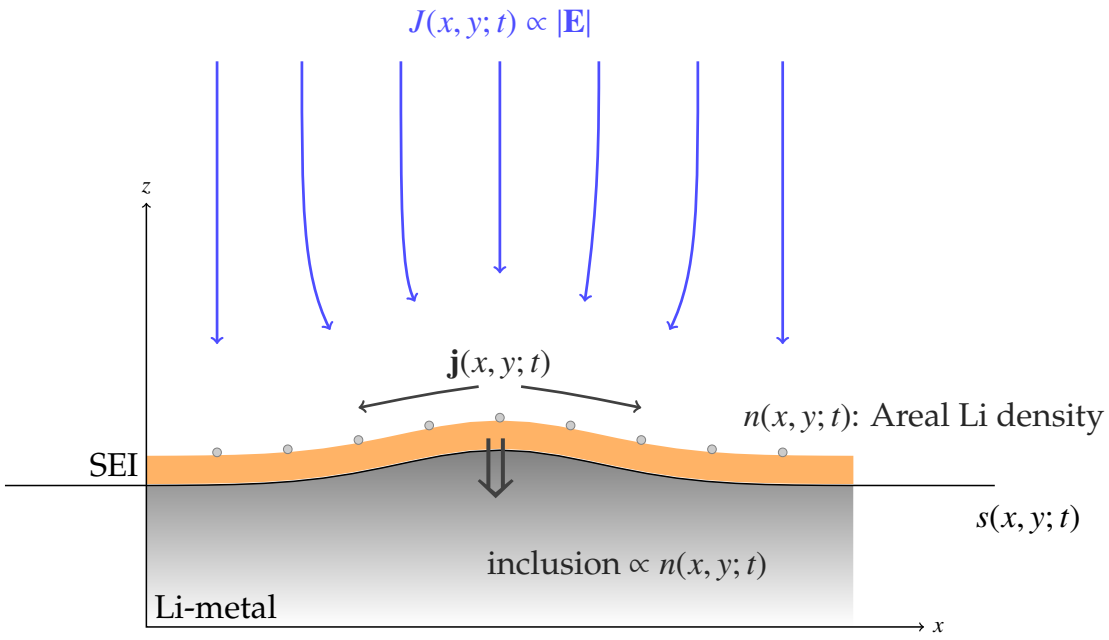

Figure 2.3: Cartoon representation of electrode surface and the terms in our macroscopic model.

sumed constant in thickness for simplicity, that has the same shape as the metal underneath. The goal of our analysis is to conclude if $s(t)$ evolves suppressing any initial irregularities on the surface or not. Here we would like to emphasize that in this formulation, we are trying to understand the initial stage of any protrusion where it does not look like dendrites yet. Karpov et al. investigated the nucleation of needle-like structures in the different context of phase change memory systems.[47, 48] In their work, they estimate the change in the nucleation barrier of the conducting phase in the presence of a field enhancing thin cylinder, similar to dendrites, already formed inside the non-conducting amorphous bulk.

The main mechanism that drives the system out of the stable regime where the metal grows uniformly is the concentrated electric field lines on the tip of any protrusion. This results in a larger *flux* (here we use the term flux for *flow rate per unit area* rather than electric flux even though they are assumed to be proportional) and faster growth at the tip. The rate at which metal atoms move sideways on the surface (xy-plane) is important as it can compete with the non-uniform deposition. If the atoms are more mobile, then they can remove any concentration gradient on the surface more efficiently through a faster random walk process. Also as the surface with irregularities costs more energy (due to the surface energy term), the mobility determines how fast the surface heals itself by removing any curvature and becoming flat.

To quantify these ideas, we start our analysis with the continuity equation:

$$\partial_t n + \boldsymbol{\nabla} \cdot \mathbf{j} = J - \nu_{\mathrm{b}} n \tag{2.3}$$

Lithium/sodium depositing on top of the SEI, creates an areal number density, $n(x, y; t)$. The surface diffusion and driving forces result in a surface current, $\mathbf{j}(x, y; t)$. $J(x, y; t)$ is the (potentially) non-uniform deposition onto the surface and the last term ($\nu_{\mathrm{b}} n$) represent the incorporation of the adsorbed atoms to the metal underneath. ν_{b} is the rate at which the lithium/sodium atoms leave the surface moving towards the metal. We then write the time evolution of surface as:

$$\partial_t s = \nu_{\mathrm{b}} a^3 n \tag{2.4}$$

where a^3 is the volume corresponding to a metal atom.

To the zeroth order, the surface is flat, and the growth is uniform. In that

limit, $J(x,y;t) = J_0$ is constant, $\boldsymbol{\nabla} \cdot \mathbf{j} = 0$, and the steady state solution where $\partial_t n = 0$ gives $n(x,y;t) = n_0 = J_0/\nu_\mathrm{b}$.

We want to subtract this overall growth and focus our attention to the irregularities. We redefine

$$\begin{aligned} n(x,y;t) &= n_0 + \tilde{n}(x,y;t) \\ J(x,y;t) &= J_0 + \tilde{J}(x,y;t) \\ s(x,y;t) &= \nu_\mathrm{b} a^3 n_0 t + \tilde{s}(x,y;t) \end{aligned} \tag{2.5}$$

We can now rewrite Eq. 2.3 and Eq. 2.4 in terms of the perturbations:

$$\begin{aligned} \partial_t \tilde{n} + \boldsymbol{\nabla} \cdot \mathbf{j} &= \tilde{J} - \nu_\mathrm{b} \tilde{n} \\ \partial_t \tilde{s} &= \nu_\mathrm{b} a^3 \tilde{n} \end{aligned} \tag{2.6}$$

The surface current incorporates two terms: the diffusion due to the random walk, and the energetics that depend on the shape. Using Fick's first law with the advection term, we write

$$\mathbf{j} = -D\boldsymbol{\nabla} n - n\,\mu\boldsymbol{\nabla}\epsilon \tag{2.7}$$

D is the surface diffusion coefficient, μ is the surface mobility, and $-\boldsymbol{\nabla}\epsilon$ is the force on the Li due to the surface tension. Surface energy cost of having a small surface perturbation $\tilde{s}$ is approximately

$$E_\mathrm{surf}[\tilde{s}] \approx \sigma \int dxdy \left(1 + \frac{1}{2}|\boldsymbol{\nabla}\tilde{s}|^2\right) \tag{2.8}$$

By taking the functional derivative of the surface energy with respect to $\tilde{s}$, we find the energy cost ϵ of adding another atom at a location where the surface shape is given by $s(x,y)$ as

$$\epsilon = -a^3\sigma\boldsymbol{\nabla}^2\tilde{s} \tag{2.9}$$

We note that this term intuitively has the right behaviour as the energy is higher where the curvature is negative (tip of a protrusion) and it is lower where the curvature is positive (bases of dendrites). Eq. 2.6 then can be written as:

$$\begin{aligned} \partial_t\tilde{n} - D\boldsymbol{\nabla}^2\tilde{n} + nma^3\sigma\boldsymbol{\nabla}^4\tilde{s} &= \tilde{J} - \nu_{\mathrm{b}}\tilde{n} \\ \partial_t\tilde{s} &= \nu_{\mathrm{b}}a^3\tilde{n} \end{aligned} \tag{2.10}$$

The next step is to write $\tilde{J}(x, y; t)$ in a way that quantifies the concentrated deposition on the tip of a protrusion. We start by writing the screened Poisson equation and solving for the electrostatic potential that satisfies the boundary condition (constant at the surface, $\phi\,(z = s(x, y)) = \phi_0$). Then we calculate the magnitude of the electric field at the surface as a function of the shape which we then relate to flux J. The screened Poisson equation reads

$$\boldsymbol{\nabla}^2\phi - \kappa^2\phi = 0 \tag{2.11}$$

where κ^{-1} is the Debye screening length.

For simplicity we assume that the irregularity lies in one dimension such that

$$\tilde{s}(x) = s_0 \cos kx \tag{2.12}$$

where s_0 is small compared to κ^{-1} or k^{-1}. Now we have constant ϕ at $z = \tilde{s}$ as our boundary conditions. It is straight forward to generalize this condition for an arbitrary wave vector $\mathbf{k}$ that lies on xy-plane as the screened Poisson equation is linear. The solution with correct behavior is given by:

$$\phi(x, z) = A\left(e^{-\kappa z} + \kappa s_0 e^{-\lambda z}\cos kx\right) \tag{2.13}$$

This form satisfies the differential equation with the condition:

$$\lambda^2 = \kappa^2 + k^2 \tag{2.14}$$

Assuming $\lambda\tilde{s} \ll 1$, it also satisfies the boundary condition at $z = \tilde{s}(x)$ to the first order. When we evaluate the magnitude of the electric field and expand the expression for small k/κ (long wavelength) we get

$$\begin{aligned} |\mathbf{E}(x, z = \tilde{s})| &= A\kappa - A\kappa\frac{k^2\tilde{s}}{2\kappa} \\ &= E_0 - \frac{E_0}{2\kappa}\boldsymbol{\nabla}^2\tilde{s} \end{aligned} \tag{2.15}$$

Using the Ohm's law ($J \propto E$)

$$\tilde{J} = -\frac{J_0}{2\kappa}\boldsymbol{\nabla}^2\tilde{s} \equiv -\chi\boldsymbol{\nabla}^2\tilde{s} \tag{2.16}$$

Hence, $\tilde{J}$ is proportional to $-\boldsymbol{\nabla}^2\tilde{s}$ which shows the predicted behavior. When the surface is concave, $\tilde{J} > 0$ and when the surface is convex, $\tilde{J} < 0$. This is the only term we have that can drive the system away from the stable regime.

Now we have all the terms to analyze the stability of $\tilde{s}$. In order to do that, we rewrite the spatial dependence of Eq. 2.10 in Fourier space:

$$\begin{aligned} \partial_t\tilde{n} + Dk^2\tilde{n} + n_0\mu a^3\sigma k^4\tilde{s} &= \chi k^2\tilde{s} - \nu_b\tilde{n} \\ \partial_t\tilde{s} &= \nu_b a^3\tilde{n} \end{aligned} \tag{2.17}$$

Combining these two equations by replacing $\tilde{n}$ gives

$$\partial_t^2\tilde{s} + (Dk^2 + \nu_b)\partial_t\tilde{s} + \left(n_0\mu a^3\sigma k^4 - \chi k^2\right)\nu_b a^3\tilde{s} = 0 \tag{2.18}$$

Guessing the solution to be in form $\tilde{s}_k(t) \propto e^{\alpha_k t}$ leads to two stable solutions only if

$$k^2 > \frac{\nu_b}{2\kappa\mu a^3\sigma}\,. \tag{2.19}$$

This analysis gives the largest instable wavenumber, hence the smallest length-scale of the instable protrusion. To avoid the dendrites, one should pick a surface which yields a large critical length. This translates into, as the Eq. 2.19 suggests a higher surface mobility μ (hence the lower surface diffusion barrier) and a higher surface energy σ.

2.2.2 Estimating the critical size of surface irregularities

In order to evaluate Eq. 2.19 for different SEI materials, we use a combination of results from *ab initio* calculations and experiments. For the screening length (κ^{-1}), we use the Debye length of a monovalent electrolyte of concentration 1 M. We choose the dielectric constant of propylene carbonate which is a typical organic solvent that is used in battery applications. For a, we take the cubic root of the volume associated with a single lithium atom and this volume is calculated as the volume of the unit cell divided by the number of lithium atoms in it. Surface energy (σ) and the surface mobility (μ) terms are the results of *ab-initio* calculations.

The inclusion rate (ν_b) is the rate at which the surface adatoms make a jump and get included into the bulk. The exact mechanism of this event is unknown to the authors by the time of this study. We estimate this rate by assuming an Arrhenius process with an energy barrier E_{inc}. After the substitutions and relating the mobility to the surface diffusion barrier E_{diff}, the critical size for the protrusions is given by,

$$l = \sqrt{\frac{2\pi^2 a^5 \kappa \sigma}{k_B T}} \exp\left(-\frac{E_{\text{diff}} - E_{\text{inc}}}{2k_B T}\right). \tag{2.20}$$

When we plug in the numerical values and take the bulk diffusion barriers of the materials to represent E_{inc}, the results are quite impressive. This model gives 45 µm for the LiF, which is within the range that is reported for the observed dendrite tips as a result of *postmortem* measurements.[58] For Li_2CO_3, we get a smaller size, around 1 µm, and for LiBr we get a macroscopic size around 1 mm.

At this point, we should note that this model assumes small current densities and that is why the current at which the electrode is driven does not appear in the equation. In a more realistic scenario, the current density plays a crucial role in the nucleation of the protrusions. In our model, the average two dimensional density of the adatoms is related to the current density and the inclusion rate ($n_0 = J_0/\nu_b$). The requirement for not allowing the incoming atoms to pile up on the surface limits the average current density that this model is valid for. We assume that the time for an adatom jumping into the bulk is much smaller compared to the time for another ion to deposit on the surface around the same location. It is the rate at which an instability grows that depends on the average current density.

2.2.3 Predictions for battery performance

Figure 2.4 summarizes all of our results including surface diffusion barriers and the surface energies, for various SEI materials. The data show that the presence of the electrolyte has significant impact, especially on the surface diffusion barriers. The surface energies of all ionic crystals go down (often by 5 – 15%), owing to the strong electrostatic interaction between the surface and the solvent. The surface diffusion barriers, however, change more dramatically, by up

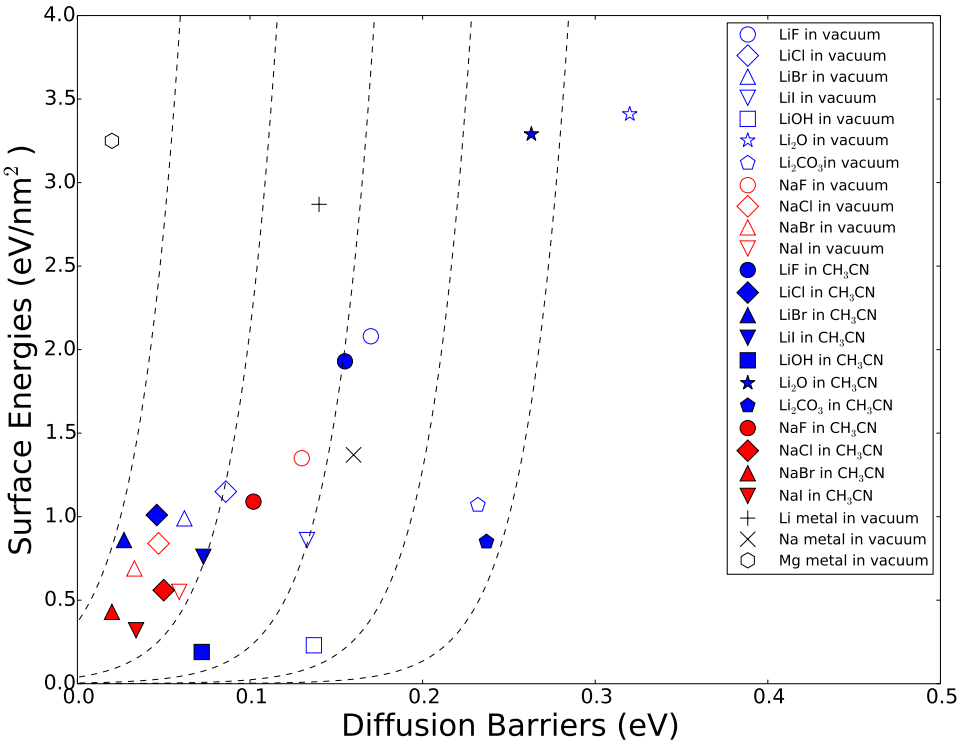

Figure 2.4: The surface diffusion barrier (x-axis) and the surface energy (y-axis) of various SEI materials. Hollow data points represent surfaces in contact with vacuum whereas filled data points represent the same surfaces in contact with the electrolyte (CH_3CN, modeled with nonlinear polarizable continuum model). The blue markers point out lithium compounds, the red ones are reserved for sodium. The black markers indicate the bare metal calculations by Jäckle and Groß. [40] The dashed curves are constant protrusion size (l) lines according to Eq. 2.20.

to as much as a factor of 2. The diffusion barrier for all materials but a couple (NaCl, Li_2CO_3) decrease when the electrolyte is included in the calculation. These changes in diffusion barriers are significant because the rate depends exponentially on the barrier height and because these energy changes are on the order of several k_BT (which, at room temperature is approximately 0.025 eV).

The data also suggest a strong positive correlation between surface energies and surface diffusion barriers for most, but not all, SEI materials. The most severe trend breakers are Magnesium metal (black hexagon), lithium metal (black plus) and LiOH (blue square). Of these, the metals break the trend likely due to their very different electronic structure, where Li is not in an oxidized (positively charged) state. LiOH likely breaks the trend because its layered structure and large intra-layer distance cause it to have a very low surface energy along the z-axis.

Li_2CO_3, present in the SEI layer formed in the presence of many commonly used electrolytes (propylene carbonate, ethylene carbonate and others), is a less severe trend breaker. It has low surface energy and high diffusion barrier, both of which are undesirable quantities in a SEI material. Lithium halides, on the other hand, have lower surface diffusion barriers than Li_2CO_3 while also having either equal or higher surface energies. Our hypothesis, first put forth in an earlier work, [31] is that the low barriers may help explain the experimentally observed phenomenon[58] in which the formation of an lithium-halide SEI is effective in suppressing dendrites. We further hypothesize that these mechanisms may be relevant not only in experiments where the electrolyte has been seeded with a Li-halide crystal, [58] but also in experiments where other additives containing fluorine (e.g. hydrofloric acid or fluoroethylene carbonate) [45, 51, 64]

have been used to improve stability and suppress dendritic growth.

As for LiOH and Li_2O, which are also occasionally observed in experiments, [58] LiOH appears to be undesirable because of its low surface energy, whereas Li_2O appears to be undesirable because of its high diffusion barrier. However, the superiority of Li-halides over LiOH/Li_2O is not as conclusive because the halides are superior in only one of the two indicators.

Finally, among halides, figure 2.4 shows that the stability (i.e. surface energy) decreases as one goes down the column of the periodic table, from F to Cl to Br to I. This is likely due to some combination of the decrease in the electronegativity of the ions (which weakens the strength of the ionic bonds) and the steric interactions increasing the size of the lattice (which decreases the electrostatic stability of the lattice). Decreased stability is an undesirable property in battery materials as it tends to lower the voltage at which the surface breaks down.

2.2.4 Change in the binding sites of alkali-halides

We find that of all the SEI materials we have studied, the halides are the most promising from the above point of view, with diffusion barriers ranging from 0.03 to 0.15 eV. The physical reasons for these low barriers are as follows. Even though the bulk structure of all the alkali-halide materials we consider here is the same (rocksalt), the binding site for adatoms changes as the anion size increases. For halides with small anions (F and Cl) the binding site for the adatom is directly above the anion ("anion site"), and in the transition state for diffusion, the adatom sits between two anions and two cations ("in-between site"). See Figure 2.5 (a) for an illustration. On the contrary, for large anions, the roles of these two sites are reversed and the binding site sits at the "in-between site"

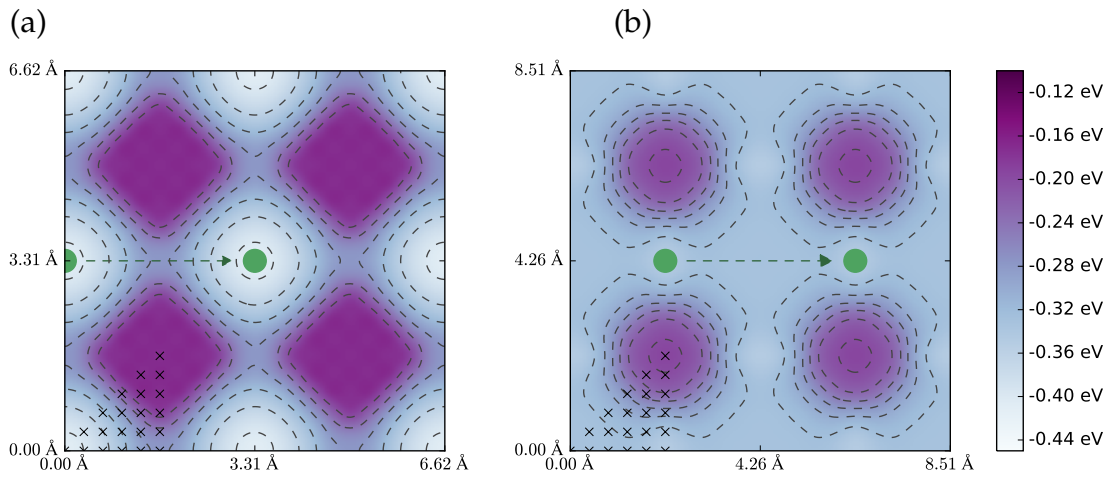

Figure 2.5: Surface binding energies versus its binding site. NaF is in the left, NaBr is on the right. The lowest energy binding sites are indicated with a green circle and the diffusion path is as shown with the green arrows. We should note that the binding energy of LiF and LiBr shows the same behavior.The black cross markers indicate our data points, the whole contour plot is generated using symmetries of the surface and cubic interpolation.

while the transition state has the adatom at the "anion site". (See Figure 2.5 (b))

The diffusion barrier is equal to the absolute value of the energy difference between the anion site and the in-between site. Because of this, halide surfaces that are in the neighborhood of this switching (Cl and Br), where the sign of this difference changes, have very low diffusion barriers. On the other hand, fluorides, which is far from this change, have a relatively larger barrier, but still small compared to non-halide SEI materials.

The reason for the change in the binding site with anion size is steric interactions. For the two smaller halogens, the in-between site is too close to the two cations, which makes it less energetically favorable. However, as the anions get bigger, the distance from the in-between site to the cations increases and the

adatom prefers to place itself in this halfway point where it can also interact with two anions simultaneously. Finally we note that even though the binding site changes as one goes down in the periodic table, the diffusion path remains the same.

2.3 Conclusion

Recent experiments, prompted by earlier theoretical work, [31] confirm the success of lithium-halide additives in suppressing dendrite growth, [58–60] consistent with the findings of previous experiments with other fluoride-containing electrolyte additives. [45, 51, 64] Prompted by this, we set out to explore more deeply the mechanisms of dendrite suppression at the atomic level.

We develop a macroscopic model to understand the kinetics of dendritic nucleation. This model captures the undesired effect of concentrated electric field lines as a source of instability. We consider the surface mobility with the surface energy as factors that smooth the surface out. Under the light of this model, we perform density-functional calculations to determine the surface energies and the surface diffusion barriers of solid-electrolyte interface materials. Our calculations show that alkali-halide SEI layers, particularly bromides, result in increased stability of the surface (higher surface energy) or higher mobility along the surface (lower surface diffusion barrier for adatoms), both of which are likely important in explaining the above phenomenon. Furthermore, our results provide an explanation for the unusually low diffusion barriers on some of the halide surfaces, tracing this effect back to a change in the binding site. This change in binding site, in turn, is driven by the trends in the electronegativity

and the sizes of the anions in the halide crystals.

This work, which focused on solid-electrolyte interphase materials, leaves many directions yet to be explored. In mitigating dendrite growth, multiple diffusion pathways are available, including surface diffusion, bulk diffusion, and diffusion at the SEI-metal interface. A study similar to this one, but for the SEI-metal interface, would be illuminating.

CHAPTER 3

AB INITIO INVESTIGATION OF NIOBIUM-TIN COATING PROCESS

State-of-the-art particle accelerators use superconducting radio frequency resonators, which for decades have been manufactured from niobium[49, 71]. The advantages of Nb are its high critical temperature and high critical magnetic field among the pure metal alternatives. There are compounds with larger transition temperatures, like high-T_c superconductors, but in addition to the practical difficulties of shaping these ceramics, they also cannot perform as well as Nb when it comes to AC applications. Radio-frequency cavities require low surface resistance to increase the quality factor (Q), cutting down the cryogenic costs which is the main expense of operating these resonators. The theoretical limit of Nb has almost been achieved, with surface treatments that have been shown to enhance the performance above these intrinsic limits[28]. A good replacement of Nb should then have a better Q-factor by having a higher T_c, higher H_c and a symmetric gap is preferred.

Nb_3Sn is a type-II superconductor discovered in 1954 with a critical temperature of 18 K[62]. Its relatively high critical temperature makes it suitable to replace the use of pure niobium in superconducting radio frequency (SRF) applications[37, 50]. The quality factor is an order of magnitude larger compared to pure Nb in low accelerating fields[36]. Although historically the high field Q-factor was severely reduced by the onset of a ”Q-slope”, recent advances in the development of the material demonstrated that this phenomenon was not intrinsic to the material, and that Nb_3Sn cavities free of high field Q-slope can be produced [80].

The recipe to grow the Nb_3Sn for SRF applications involves Sn vapor de-

position on Nb surfaces at elevated temperatures around 1200°C. Researchers reported that this process also results in regions of lower Sn percentage (~17%) within Nb_3Sn layer. Due to the lower T_c of this mixture ratio, this defect is suggested as the root cause of the high surface resistance[9]. While the low Sn concentration regions are not the only defects that have been observed, in order to optimize the production procedure we need more insight on the microscopic mechanism by which the Nb_3Sn layer grows. We use *ab initio* calculations to shed light on this process, building on the previous work done in this direction. [10, 72, 101]

3.1 Computational Methods

For the first principle DFT calculations, we use the JDFTx software[89] implementing Kohn-Sham density functional theory in the plane wave basis. We employ norm-conserving Trouiller-Martins type pseudopotentials[97] taken from the Fritz-Haber-Institute library[23]. Nb and Sn pseudopotentials have five ($5s^2 4d^3$) and four ($5s^2 5p^2$) valence electrons respectively. The fermionic exchange energy and the effect electron correlations are approximated in the generalized gradient approximation scheme using PBE parametrization[75].

The energy cutoff for the plane-wave basis was 25 E_h, and for geometry optimizations, the atomic coordinates were relaxed until the RMS of the forces were below 1 mE_h/a_0. For the Brillouin zone integration, we use a Monkhorst-Pack mesh that is converged to 1 mE_h. This corresponds to a $6\times6\times6$ grid for the unit cell of Nb_3Sn (which contains eight atoms).

We utilize the nudged elastic band technique to optimize the energy bar-

	This work	Experimental vaue	% difference
Nb lattice constant (BCC)	$6.28\,a_0$	$6.24\,a_0$	1%
Nb bulk modulus	171 GPa	170 GPa	0.6%
α-Sn lattice constant	$8.89\,a_0$	$8.65\,a_0$	2.8%
α-Sn bulk modulus	36.7 GPa	(38.5 GPa)	5.2%
β-Sn lattice constant	$11.2\,a_0$	$11.0\,a_0$	1.8%
Nb_3Sn lattice constant	$10.06\,a_0$	$9.99\,a_0$	0.7%

Table 3.1: Validation of our computational methods[17, 83, 93]. Value in parenthesis is result of other first principle calculations in the literature [42]

rier on the continuous transition pathways as it is implemented in ASE [7, 43]. The python binding of JDFTx (pythonJDFTx) [70] provides a force calculator that keeps the wave functions and the electronic densities in memory while optimizing the atomic positions. This results in a performance advantage when compared to traditional external force calculators that read and write to the disk for the same communication.

We run lattice optimizations to test the pseudopotentials and the rest of our computational parameters. As a sanity check, we compare them to the experimental measurements or to the existing first principle calculations (Table 3.1).

3.2 Initial nucleation of Nb_3Sn

One of the areas of experimental interest concerns the initial nucleation of Nb_3Sn. The vapor deposition method, which has to date produced best coating for RF applications, involves many steps that still lack a fundamental microscopic understanding, one of which is the effect of the nucleation agent.

The first attempts of vapor deposition directly on Nb surface resulted in re-

gions without Nb_3Sn coating. In order to prevent these regions, two methods have been used, anodizing the Nb surface, and the use of a nucleation agent like tin-chloride or tin-fluoride. The anodization method became unpopular because by the end of the coating process, the oxygen diffuses into the bulk Nb decreasing its purity.

The common belief is that the mixing is enhanced by diffusion along the grain boundaries of the Nb_3Sn layer. However ,it is uncertain if the species undergoing diffusion is Sn, Nb or both. To attack this question, we calculate the substitutional defect energies in bulk Nb and Sn crystals. The changing stoichiometry was accounted for by the use of bulk energies as reference. This reference energy corresponds to the chemical potential of the substituting atom in the regular grand canonical ensemble picture. To be clearer:

$$E_{\text{subs}}(\text{X}_\text{Y}) = E_{\text{supercell}}(\text{XY}_M) - E_{\text{bulk}}(X) - M \times E_{\text{bulk}}(Y) \tag{3.1}$$

where X_Y denotes the substitution of X in Y lattice and XY_M is the chemical formula of the supercell, a Y lattice which contains X as a substitution. The results are:

$$E_{\text{subs}}(\text{Nb}_\text{Sn}) = \quad 2.96\,\text{eV}$$
$$E_{\text{subs}}(\text{Sn}_\text{Nb}) = -0.85\,\text{eV}$$

The negative energy of Sn substituting into the BCC Nb suggests that energetically Sn wants to form a substitutional defect in Nb instead of forming a bulk Sn structure. This is why we believe that it is the tin moving into niobium to form Nb_3Sn, not the other way around. At this point, it is worth noting that the α-Sn structure is used as reference, although the β-Sn also gives a negative

substitutional energy. This reasoning however does not take into account the dynamics of the diffusion.

3.3 Transformation from BCC to A15

The A15 phase is the preferred structure for alloys like Cr_3Si, V_3Ga and also for Nb_3Sn. In this structure, Sn atoms form a BCC sublattice and Nb atoms form lines along the faces of the BCC sublattice. Tungsten, normally having a BCC structure, experiences A15 as a meta-stable phase known as β-W. So this structure is not specific to binary alloys. In fact, for bulk molybdenum, which is found in BCC form in its ground state, the A15 configuration is only slightly higher in energy and is a competing phase.

Since our results indicate that a binary system consisting of a mixture of bulk Nb and bulk Sn can reduce its energy by placing Sn atoms as substitutions in BCC niobium, a further relaxation must be available by changing the lattice from BCC to A15. The lowest energy transition of this type is predicted by Xiao et al. for Mo crystals [104], which constitutes the starting point of our investigation.

We begin by taking a supercell of BCC structure in which both the lattice vectors and the atomic coordinates match relatively well with A15 configuration. Xiao et al. gives two different representations of the BCC structure that can be transformed into A15 with a relatively small change.

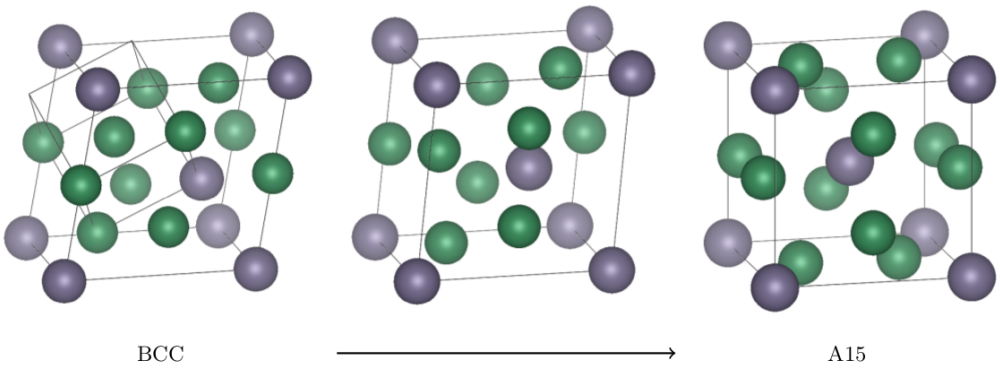

Figure 3.1: BCC to A15 transition - the first pathway. Replicated atoms outside of the unit cell are also shown on the first picture to be able to sketch the edges of the cubic BCC.

3.3.1 First pathway

The illustration of the first transition is given in Figure 3.1. For further reference, the atomic positions are given in Table 3.2. The supercell in the BCC configuration has the lattice vectors ($^{3}/_{2}$, $^{-1}/_{2}$, $^{-1}/_{2}$), (1, 1, 1) and (0, -1, 1) in terms of a cubic representation of BCC lattice vectors. The length of these three vectors are %3.6, %8.2 and -%11.2 different from the A15 lattice constant of Nb_3Sn. These numbers correspond to normal strain values of the Nb_3Sn crystal right after the appropriate substitutions. There is also a $\sim 10^{\circ}$ shear as the first two vectors are not orthogonal.

We would like to note that the lattice mismatch is greatest in the third direction and it is normal to the (110) surface of a BCC. Among low index Nb surfaces, the (110) surface is the lowest energy surface.[52] This suggests that if the transition happens at the surface, the Nb_3Sn layer can relax in the third direction decreasing the total energy.

	BCC Basis	A15 Basis	Difference
Sn	(0, 0, 0)	(0, 0, 0)	(0, 0, 0)
Sn	(¾, ⅜, ½)	(½, ½, ½)	(-¼, ⅛, 0)
Nb	(½, ¼, 0)	(½, ¼, 0)	(0, 0, 0)
Nb	(½, ¾, 0)	(½, ¾, 0)	(0, 0, 0)
Nb	(0, ½, 0)	(0, ½, ¼)	(0, 0, ¼)
Nb	(¼, ⅛, ½)	(¼, 0, ½)	(0,-⅛, 0)
Nb	(¼, ⅝, ½)	(0, ½, ¾)	(-¼,-⅛, ¼)
Nb	(¾, ⅞, ½)	(¾, 1, ½)	(0, ⅛, 0)

Table 3.2: Fractional coordinates for two unit cells: BCC supercell and A15 primitive cell. They are visualized in Figure 3.1.

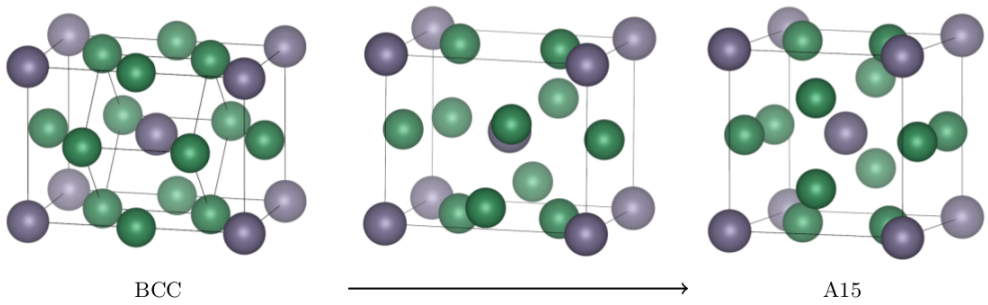

Figure 3.2: BCC to A15 transition - the second pathway. The edges of the cubic BCC is also shown.

3.3.2 Second pathway

Figure 3.2 shows the second transition. The supercell lattice vectors are (2, 0, 0), (0, 1, 1) and (0, -1, 1). The internal coordinates are listed Table 3.3. As the lattice is tetragonal, there is no shear involved after the substitutions. The normal strains are 24.9%, and -11.7%. The higher strain direction is the (100) direction of the BCC Nb structure.

	BCC Basis	A15 Basis	Difference
Sn	(0, 0, 0)	(0, 0, 0)	(0, 0, 0)
Sn	(½, ½, ½)	(½, ½, ½)	(0, 0, 0)
Nb	(¼, ½, 0)	(¼, ½, 0)	(0, 0, 0)
Nb	(¾, ½, 0)	(¾, ½, 0)	(0, 0, 0)
Nb	(0, ½, ½)	(0, ¼, ½)	(0,-¼, 0)
Nb	(¼, 1, ½)	(0, ¾, ½)	(-¼,-¼, 0)
Nb	(½, 0, 0)	(½, 0, ¼)	(0, 0, ¼)
Nb	(¾, 0, ½)	(½, 0, ¾)	(-¼, 0, ¼)

Table 3.3: Fractional coordinates for the 2nd transition pathway shown in Figure 3.2.

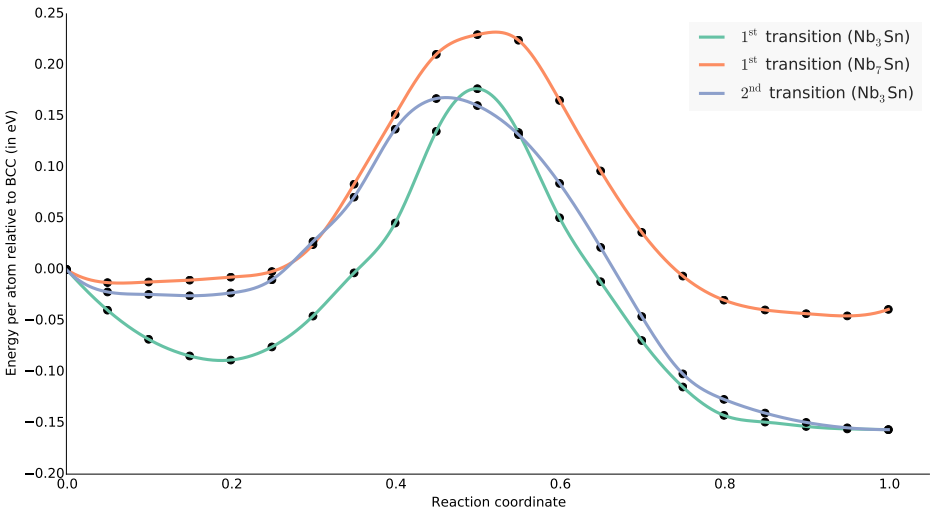

Figure 3.3: Energy per atom as a function of reaction coordinate. The height of the barrier gives the transition energy.

3.3.3 Transition Energies

For the two transition pathways, we run nudged elastic band (NEB) calculations in order to converge to the lowest energy barrier for the two transitions. However, the NEB relaxation was over the atomic positions only, while the lattice vectors of the image points are linearly interpolated between end-points. Figure 3.3 shows the resulting energy barrier. The two transitions have similar energy barriers, 0.18 eV for the first transition and 0.17 eV for the second. We also calculated the transition energy of a Nb_7Sn unit cell from BCC structure to A15, corresponding to a switching in the lattice structure after one Sn substitution into bulk Nb.

For the first transition pathway, we see that the BCC internal coordinates are not stable right after the substitutions. It is able to relax if we let it break the symmetry of the BCC lattice.

3.4 Ab initio study of Nb-Nb_3Sn interface

The low energy transitions that we present in the previous section can also be used to study the a BCC-A15 interface. A stable Nb-Nb_3Sn interface can be used to infer the nature of the diffusion mechanism by which Sn diffuses into bulk Nb forming Nb_3Sn.

The key question that needs to be answered is what the lattice match is between bulk Nb and the Nb_3Sn layer. In our attempt to find a stable interface, we fixed the BCC Nb lattice vectors and squeezed the Nb_3Sn lattice vectors to match the underlying Nb crystal. With the strain values from the first transition

it appears that the A15 internal coordinates are higher in energy compared to the BCC internal coordinates. In other words, when we relax the Nb_3Sn layer sitting on top of a bulk Nb layer following the underlying lattice vectors along the plane, the strained A15 structure is unstable. Further study regarding this problem is needed for a better lattice match which requires a larger unit cell and more computation time.

3.5 Conclusion

Nb_3Sn is a very promising candidate to be the successor of Nb for superconducting radio frequency applications in particle accelerators. The performance of this alternative material still falls short of its theoretical maximum due to defects introduced by the current fabrication process. More research is being invested to push Nb_3Sn towards its theoretical potential, which if successful will significantly lower the cost of SRF applications.

In this chapter we studied, from the first principles, the microscopic mechanism by which the Nb_3Sn coating is grown on top of bulk Nb surface. Substitutional defect energies suggest that with bulk reference energies, Sn substitutions into bulk Nb decreases the energy, suggesting that Sn diffusion is the dominant mechanism by which these two substances mix. We then presented two low energy transition mechanism connecting the BCC to the A15 structure in the configuration space. These transitions form potential candidates for a good lattice match and a future study of Nb Nb_3Sn interface.

A reasonable follow up to the *ab initio* study we presented here would be the one that sheds light on the grain boundary diffusion. The Nb_3Sn layer usually

forms lots of small grains regardless of the average size of Nb grains. The reason for this is not fully understood. Furthermore, there have been observed regions of larger Nb_3Sn grains, associated with a limited diffusion and thinner coating. The thickness of these regions goes down to the level of the penetration depth of the radio frequency field causing a performance bottleneck. In order to prevent this phenomenon, a microscopic understanding of grain boundary dynamics would be helpful.

CHAPTER 4

RARE EVENT DYNAMICS WITH JOINT DENSITY-FUNCTIONAL THEORY

Molecular dynamics (MD) is the simulation technique to generate time trajectories of atoms and molecules by the integration of Newton's equations. It gives the ability to study many body systems in the microscopic level and observe thermodynamic properties by the means of computer simulations. *Ab initio* molecular dynamics (AIMD) is the flavor of MD in which the forces are results of an electronic calculation. The electronic description of the system makes it possible to capture the chemical events like charge transfer, bond forming/breaking but comes with the extra computational cost.[61]

The force calculation methods range from relatively cheap molecular mechanics force fields all the way to the computationally expensive quantum chemistry techniques like Møller-Plesset perturbation theory. Given some amount of computational resources, the choice of the method sets a limit on how large of a microscopic system can be defined, or on how long it is feasible to run the simulation. Computational time for DFT, the most widely used method among the AIMD techniques, scales cubically with the size of the simulation cell. This means, when we apply Moore's law (which says computer power doubles every 1.5 year), we have to wait 4.5 years in order to study a system that is double the size of the system that is currently available.

Instead of ameliorating the scaling, Car-Parinello molecular dynamics (CPMD)[13] separates the timescales of nuclear and electronic motion in order to improve on the prefactor. Instead of constraining the trajectories to the Born-Oppenheimer (BO) surface by minimizing over the electronic degrees of free-

dom between the time steps, CPMD propagates the wave functions according to fictitious dynamics. This method deviates from the BO surface but by carefully tuning the fictitious mass assigned to the electronic degrees of freedom, the electronic and nuclear systems are almost decoupled. Due to this separation, energy flow from the hot nuclei to the cold electronic system does not happen within the time scale of the simulation. However, if we bypass the minimization steps between the time steps using CPMD, we now have to shrink the time step and this reduces the performance gain. Herr and Steele showed that by choosing the initial conditions for the minimization cycles, it is possible to decrease the required number of iterations significantly. [35] (They report ~ 3 times faster convergence)

Order N DFT has also gained traction as it improves upon the scaling factor. It uses the locality of electronic structure and exploits the sparsity of the Hamiltonian. Its linear scaling is certainly a great promise to increase the range of simulations that are computationally accessible but it lags behind other methods in robustness and accuracy.[5, 12, 65]

Hybrid methods, often noted as QM/MM, which separates the simulation domain into two parts, are very popular in studying large systems. The chemically active region is described by electronic (QM) means, and the surroundings are described in molecular mechanics (MM) level. These methods are limited by arbitrariness in the choice of th coupling of two regions and also subtleties in capturing the physics at the QM-MM interface.

Joint density functional theory is an in principle exact method to incorporate the effect of the fluid environment on the electronically described solute system. It is a mean field theory that removes the need to sample many micro-

scopic configurations to accurately estimate the thermodynamic averages. As implementations of JDFT scales linearly with the system size, it is possible to accelerate AIMD simulations using JDFT to describe fluid environment. For rare event dynamics in particular, where the thermodynamically averaged free energies are the fundamental quantities that the rates depend on, directly substituting the explicit atoms with JDFT description can enhance the performance without effecting the accuracy. In this chapter, we will first set the theoretical framework and explain how JDFT dynamics can reproduce the correct rare event time scales and mechanics. We then talk about certain practical issues that led us to the test system we chose. We present our results after describing the computational methods used.

4.1 Theoretical Background

Transition state theory[98] (TST) is a widely accepted and successful theory that elucidates rare event dynamics like chemical reactions or diffusion. Eyring, in 1935, produced the simplest classical form of the theory starting from quasiequilibrium hypothesis.[20] Here we state Eyrings result and describe how JDFT dynamics should reproduce the same time scale for rare events in simulations.

In Figure 4.1, we sketch an arbitrary energy surface in two dimensional space for illustration purposes. We have two minima corresponding to two stable states. The red curve is drawn as a boundary between two regions associated with the local minima. Quasiequilibrium hypothesis tells us that a transition happens if and only if the system crosses the red curve, and that the rate of the transition is given by the one way probability flux across the boundary. The probability current has an exponential dependence on the height of the energy

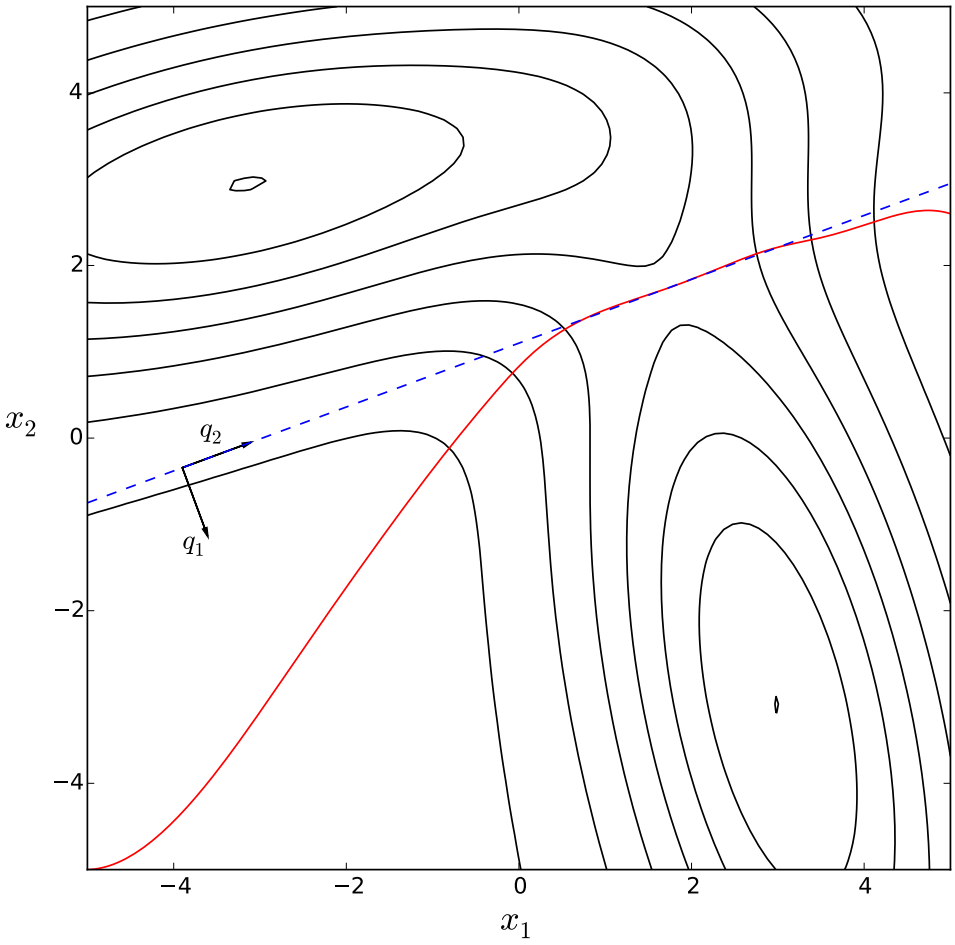

Figure 4.1: Contour plot of an arbitrary two dimensional energy surface.

barrier. Therefore, the flux is dominated by the contribution around the lowest energy point on the boundary surface, which gives the lowest energy barrier along a continuous path between the two stable minima. It is a saddle point of the energy surface; a maximum in the direction of the transition path, minimum in all other directions. Applications of TST requires accurate and efficient algorithms to find the lowest energy saddle points on the energy surface[34, 81].

Without loss of generality, among 3N generalized coordinates, we pick q_1 along the direction in which the saddle point is a maximum. We call it *the reaction coordinate* and we let $\{p_i\}$ denote the associated momenta. We define q^* to be the coordinate of the saddle point along q_1, so $q_1 = q^*$ defines the hyper surface that separates two stable minima (the blue dashed line in Figure 4.1. This flat surface is a good approximation to the curved separating surface of the quasiequilibrium hypothesis around the saddle point. The total probability flux through this hyper surface is the quantity of interest. The probability density of being on this hyper-surface, $\rho(q_1 = q^*, p_1)$ is given by

$$\begin{aligned}\rho(q_1 = q^*, p_1) &= \frac{e^{-\beta\frac{p_1^2}{2m_1}} \iint\limits_{q_2,\, p_2} dq_2 dp_2 ... \iint\limits_{q_{3N},\, p_{3N}} dq_{3N} dp_{3N}\, e^{-\beta\left\{\sum\limits_{i\neq 1}\frac{p_i^2}{2m_i} + V(q_1 = q^*,\, \{q_i\})\right\}}}{\iint\limits_{q_1,\, p_1} dq_1 dp_1 ... \iint\limits_{q_{3N},\, p_{3N}} dq_{3N} dp_{3N}\, e^{-\beta\left\{\sum\limits_{i}\frac{p_i^2}{2m_i} + V(\{q_i\})\right\}}} \\ &\equiv e^{-\beta\frac{p_1^2}{2m_1}} \frac{h^{3N-1}\, Z^\dagger}{h^{3N}\, Z}\end{aligned} \tag{4.1}$$

and the one way probability current is

$$\begin{aligned}\nu &= \int_0^\infty \frac{p_1}{m_1}\, \rho(q_1 = q^*, p_1)\, dp_1 \\ \nu &= \frac{k_B T}{h} \frac{Z^\dagger}{Z}\end{aligned} \tag{4.2}$$

Here, Z is the classical partition function, integrated over the entire phase space, and $Z^\dagger$ is the partition function after setting q_1 to q^* and p_1 to zero. In terms of free energies associated with these partition functions, we see that the rate exponentially depends on the difference:

$$\nu = \frac{k_B T}{h} e^{-\beta\left(F^{\dagger} - F\right)} \tag{4.3}$$

This result suggests that any reaction with the same free energy difference between its reactants and its activated state should happen at the same rate. Furthermore, the only significant coordinate is the reaction coordinate (q_1), assuming we do not know what q^* is, theoretically all the others can be integrated out. In other words, as long as we express the reaction coordinate in terms of explicit atomic coordinates in our MD simulations, we can average out the remaining degrees of freedom.

We propose a recipe to run AIMD simulations using JDFT to represent the fluid environment to some degree. The chemically active region, including some fluid atoms and molecules, is explicitly described and the rest of the fluid environment is expressed by its thermodynamic averages through JDFT. The purpose of fluid region with explicit atoms is to accurately describe the reaction coordinate. In the end, the partition function is separated as follows

$$Z = \underbrace{\frac{1}{h^{3M}} \iint\limits_{q_e\ p_e} dq_e^{3M} dp_e^{3M} e^{-\beta \sum \frac{p_e^2}{2m_e}}}_{\text{explicit region}} \underbrace{\frac{1}{h^{3M'}} \iint\limits_{q_f,\ p_f} dq_f^{3M'} dp_f^{3M'}\ e^{-\beta\left\{\sum \frac{p_f^2}{2m_f} + V(q_e,\, q_f)\right\}}}_{\text{JDFT region}} \tag{4.4}$$

We can see that JDFT part of the partition function integral describes an effective field as a function of q_e, the explicit atomic coordinates. We can rewrite it as Z^{JDFT}:

$$Z^{\text{JDFT}}(q_e) = \frac{1}{h^{3M'}} \iint\limits_{q_f,\ p_f} dq_f^{3M'} dp_f^{3M'}\ e^{-\beta\left\{\sum \frac{p_f^2}{2m_f} + V(q_e,\, q_f)\right\}} \equiv e^{-\beta\ V_{\text{eff}}(q_e)} \tag{4.5}$$

When we use the free energy JDFT calculates (or approximates) as the potential energy surface that explicit atoms move on, the partition function remains unchanged. Any quantity that depends only on the partition function, like the rate of rare event dynamics, can be estimated by simulating a few explicit atoms in JDFT fluid environment. The key requirement is that when the reaction coordinate is projected onto the explicit coordinates, $\{q_e\}$, it should be sufficiently well represented.

4.2 Practical Considerations

One of the shortcomings of running JDFT dynamics is the unphysical representation of the boundary between the explicit atoms and the fluid environment. The current level of JDFT cannot resolve the charge transfer or chemical reactions. More importantly, JDFT does not capture the dynamics on timescales of the response time of the fluid. This leads to a couple of issues. First, atomic vibrations at the boundary of the explicit region are do not get any response from the averaged out fluid region. As we are interested in the physics at the core of the explicit region rather than its boundary, this in itself is not big problem. But a second issue arises from the first one; the explicit atoms slowly dissolve in the JDFT fluid. Normally self diffusion of fluid molecules is also a rare event and can be studied in the same way. But the number of explicit coordinates is insufficient to accurately approximate the reaction coordinate for the diffusing boundary atoms.

In order to overcome this issue we choose the system to test our recipe carefully. We study the diffusion of OH^- in water. Hydroxyl ions move in water

via proton hopping, also called Grotthuss mechanism.[2, 18] This is a rare event that fits our description and it is fast compared to the self diffusion of water. Therefore we are able to eliminate the boundary effects in a relatively small simulation box. Furthermore the fluid functionals for water are the most well studied functionals in JDFT framework.

4.3 Computational Methods

We carried out *ab initio* molecular dynamics simulations using plane wave implementation of density functional theory, as it is coded in open source JDFTx software[89]. We used ultra-soft pseudopotentials[102] from GBRV library[26]. The energy cutoff for plane wave was 20 E_{h}. To account for exchange-correlation corrections, we used the PBE functional[75], a form of generalized gradient approximation. We chose Verlet algorithm[103] as the method of time integration and we use velocity rescaling in order to set temperature before running the simulation to collect data.

The unit cell contains 31 water molecules and one OH^- ion for the bulk fluid run. We replaced 16 water molecules with its thermodynamically averaged representation in our JDFT dynamics runs. Within JDFT framework, we used nonlinear-PCM approximation which treats the fluid environment as a dielectric and takes into account the rotational saturation of the fluid response[30]. The simulation box was a cube with edge length 9.8 Å. After setting the temperature to room temperature, we ran the bulk simulation for 37.5 ps, with a time step of 1 fs. The JDFT dynamics simulations were in total 23.7 ps long.

In order to overcome the problem of water molecules moving freely into the

JDFT fluid, we employ a fictitious gravitational-like field that pulls the explicit molecules towards the center of the simulation cell. The acceleration associated with this confining field is given by

$$\vec{a}_{\text{conf}} = -\frac{a_0}{1 + e^{-(r-r_0)/w}}\hat{r} \tag{4.6}$$

where r is the distance from the origin. The fictitious acceleration is zero near the center and it turns on exponentially around r_0 with a width w, reaching a constant strength a_0 further away from the center. This makes sure that only the boundary atoms are effected by this confining force hence the center of the droplet remains physically described.

4.4 Results

4.4.1 OH^- diffusion in explicit water

The most common way to estimate the diffusion coefficient is to look at mean square displacement (MSD) of the species of interest. We use the Brownian motion result which is

$$D = \frac{1}{2d} \lim_{t\to\infty} \frac{\left\langle \left|\vec{r}(t) - \vec{r}_0\right|^2 \right\rangle}{t} \tag{4.7}$$

where d is the dimensionality, which in our case is 3. In order to calculate the most accurate MSD, we average over multiple initial conditions in the time series data. Given $\vec{r}(t)$, we calculate

$$R(\Delta) = \left\langle \left|\vec{r}(t+\Delta) - \vec{r}(t)\right|^2 \right\rangle_t \tag{4.8}$$

and the asymptotic slope of $R(\Delta)$ vs Δ gives the diffusion constant.

The immediate problem we encounter for the system at hand is the determination of the location of OH^-. We simplified the problem by tracking the oxygen of OH^-. For each time frame, we match all the hydrogens with their closest oxygen and we identify OH^- from the oxygen that lacks the second proton.

One also needs to be careful with periodic boundary conditions, as in our bulk simulations, eventually OH^- wraps around. We tackle this by taking the displacement vectors at each time step and reflecting them to $\left[-\frac{a}{2},\frac{a}{2}\right]$ interval by a modulus operation, then reforming $\vec{r}(t)$ as the cumulative sum of the displacements.

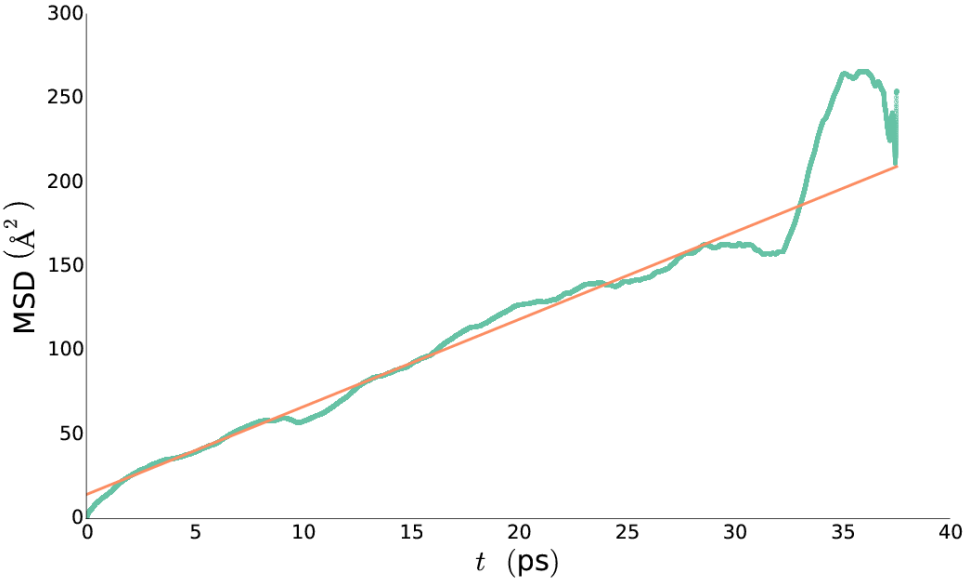

Figure 4.2: MSD for OH^- in bulk water. Green points are the data points extracted from the simulation, orange line is the line fit to the data between [2.5 ps, 30 ps] interval. This interval excludes long times, where data has high uncertainty, and also small times, where we are not in the Brownian regime for the motion of OH^-.

Figure 4.2 shows the MSD for our bulk run, OH^- diffusing in explicit water molecules. We see a clear linear trend which validates our methods. The deviations from linear regime in the tail and at the beginning are expected. For small times, the correlations are not negligible and for large times, we do not have enough data to represent the expected value of square displacement. The slope of the linear fit gives us the diffusion coefficient as 8.7×10^{-5} cm^2/s. This value is within the range of reported values [99, 100]. The water structure (or the solvation shell of OH^-) varies quite a bit depending on the choice of exchange-correlation functional, which then effects the diffusion coefficient. Since the purpose of our study is not to reproduce the experimental diffusion coefficients but to get the rare event dynamics right, getting the behavior qualitatively right is enough at this point.

4.4.2 Direct estimation of hopping times

The main rare event that we are interested is the proton hopping within the OH^- solvation shell, the Grotthuss mechanism. This is the dominant way that OH^- diffuses in water and also the reason why OH^- diffusion is much faster than the water self diffusion.

In order to compare simulations in JDFT water with the simulations in bulk water, direct estimation of mean hopping time would be a useful statistic because MSD calculations requires much longer simulations to give accurate results. In the JDFT dynamics, we are simulating a small cluster of water molecules around the OH^- and this puts an overall time limit, the time required for the OH^- to reach to the boundary of the explicit region. This maximum time

may or may not be sufficiently large to observe the linear regime of MSD, depending on the size of the cluster. The other more subtle reason for estimating hopping times lies in the fact that the OH^- diffusion has two components to it, the proton hopping and the random motion of the oxygen atoms. We want to be able to simulate the Grotthuss mechanism and isolate it from the motion of the oxygen atoms.

The way we associate the oxygens with their protons makes determination of the OH^- oxygen somewhat arbitrary especially when a jump is about to happen. Right before a jump, a proton oscillates in between two oxygens and ideally half of the times it ends up on the other oxygen, resulting in a hop. During these oscillations, our simple algorithm records many jumps even if an actual jump does not take place. That is why this naive way of estimating the average hop time by a simple ratio of time to the number of jumps recorded would not work. Just like long time dynamics is not physical for JDFT simulations, small time behavior is not very well described either. Formulation of an algorithm to separate the oscillations from actual jumps by taking into account future time frames is also subtle as it brings either more arbitrariness or bias into the picture.

We can exploit the fact that there are a lot more data points for small times and that they can describe an averaged quantity very well. In this approach, we define $P(t)$ as the probability of OH^- being associated with the same oxygen after some time t. This probability is one for $t = 0$ and it asymptotically approaches to $1/N_O$ with time, N_O being the number of oxygens in the simulation cell. We estimate this probability from our time series by averaging over initial times:

$$P(t) = \left\langle \theta(t_0 + t, t_0) \right\rangle_{t_0} \tag{4.9}$$

where $\theta(t_1, t_2)$ is defined as

$$\theta(t_1, t_2) = \begin{cases} 1, & \text{if the oxygen of } OH^- \text{ is the same at } t_1 \text{ and } t_2, \\ 0, & \text{otherwise.} \end{cases} \tag{4.10}$$

This probability reflects the small time behavior of proton hopping including the oscillations prior to a successful jump. In order to understand the physics of proton hopping further, we compare $P(t)$ obtained from our simulation with the one obtained from purely random, uncorrelated jumps on a diamond lattice.[1] We numerically solve the differential equation

$$\frac{dP(\vec{r}, t)}{dt} = -\nu P(\vec{r}, t) + \frac{\nu}{q} \sum_{\substack{\vec{\Delta}: \\ \text{neighbors}}} P(\vec{r} + \vec{\Delta}, t) \tag{4.11}$$

where q is the number of neighbors, four for the diamond lattice. The assumption is that the proton hopping is a Poisson process with a rate constant ν. Figure 4.3 shows agreement between our simulation and random jumps on a diamond lattice. Even though the oxygens in our molecular dynamics do not form an exact diamond lattice, the agreement for times after 2 ps is quite convincing. For smaller times, we are in a different regime where the dominant effect is the oscillations prior to any successful jump.

We fit to our simulation data after 2 ps, yielding a time constant of 1.23 ps. From this time constant, we can calculate a diffusion coefficient given a mean hop distance. We estimate the average hopping distance from our molecular dynamics simulation as 2.5 Å, resulting in a diffusion constant:

[1] We choose diamond lattice because the structure of OH^- and its surrounding water molecules tend to have tetrahedral bonds.

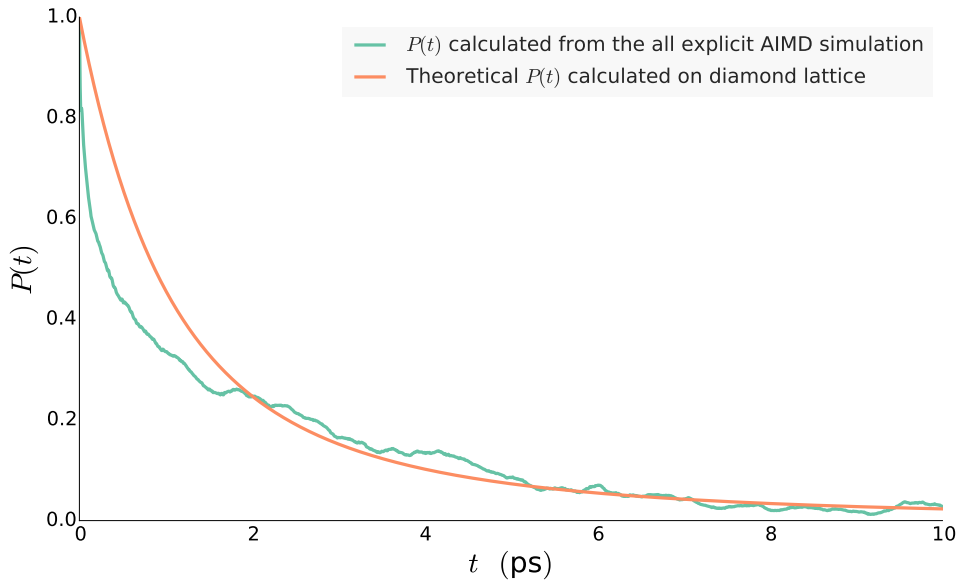

Figure 4.3: Fitting $P(t)$, the probability of finding the OH^- on the same oxygen after time t, with the Green's function solution to uncorrelated jumps on a diamond lattice.

$$D = \frac{\left\langle |\Delta\vec{r}| \right\rangle^2}{6\tau} = 8.5 \times 10^{-5} \mathrm{cm}^2/\mathrm{s} \tag{4.12}$$

The agreement between the diffusion coefficients estimated from MSD and from the hopping statistics confirms that the Grotthuss mechanism is the dominant way in which the hydroxyl ion moves in water.

4.4.3 Comparison with JDFT Dynamics

Due to practical limitations of JDFT dynamics, we cannot generate one long trajectory from a single dynamics run. When the OH^- approaches the boundary

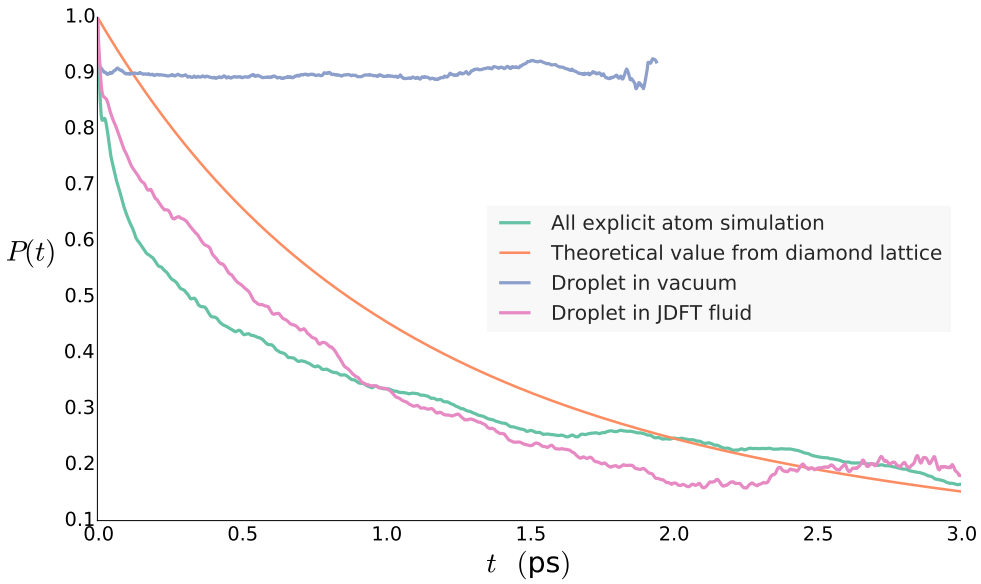

Figure 4.4: Comparison of small time statistics of various simulations

of the explicit region, the dynamics become unphysical. The size of the explicit droplet determines how long one can run the dynamics. In order to boost the statistical significance of our results, we average over seven short trajectories ($\sim$ 3.3 ps).

We also compare to the results of running the droplets in vacuum. This helps us to isolate the effect of JDFT. With the same initial conditions, the droplets in vacuum are evaluated a little longer than $\sim$ 2.0 ps. Figure 4.4 shows our results for small time statistics. As it is clearly seen, JDFT does a good job reproducing the all explicit atom hopping behavior, while the vacuum simulations do not.

Finally, we calculate the mean square displacement for the vacuum and JDFT dynamics runs We generate the MSD curves for each individual run and then fit a line to the average of the curves. In Figure 4.5, the curves in colors are included

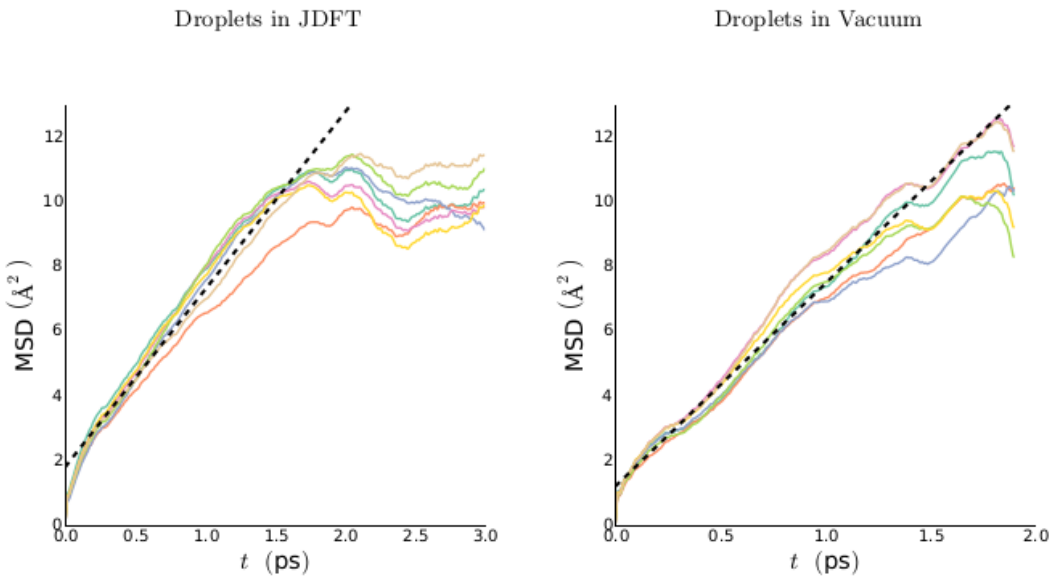

Figure 4.5: Mean square displacements averaged over multiple short simulations with different initial conditions.

to show the spread of the data. These curves themselves are also averages obtained by leaving one trajectory out. The diffusion constants calculated from the slopes of the best fit lines (shown in dashed black line) are 9.1×10^{-5} cm^2/s for the droplets in JDFT and 10.5×10^{-5} cm^2/s for the droplets in vacuum. Since the simulations in vacuum overestimate the diffusion coefficient even though the small time hop statistics indicate that the OH has a low hopping frequency, the diffusion mechanism that the vacuum runs produce is unphysical: the OH^- in vacuum does not diffuse via Grotthuss mechanism but by the random motions of the hydroxyl ion.

4.5 Conclusion

Ab initio molecular dynamics, while very accurate in the description of chemical systems, is still computationally too expensive for large systems. There exist methods that improve upon the scaling of first principle methods but they are not sufficiently stable and accurate for massive adoption. In this chapter, we proposed JDFT dynamics as a technique that is capable of reproducing the correct rare event dynamics while scaling linearly with the system size. As a proof of concept, we present how JDFT dynamics reproduces the Grotthuss mechanism and does much better job compared to simulations in vacuum.

As a future work, we would like to see a similar demonstration with more detailed fluid functionals, such as classical density functionals for fluids. There is also room for improvement in numerical minimization algorithms used for the fluid degrees of freedom in the current implementation of JDFTx software. Force calculations should carefully be studied and tested for numerical instabilities. The simulation results presented as parts of this work can also be improved by using more time and computational resource to average over more trajectories.

CHAPTER 5

CONCLUSIONS

Ab initio quantum chemistry methods have been proven very successful in explaining the microscopic details of intriguing physical phenomena and in guiding experimental and technological development. The wide range of application of these techniques along with advancements in computational resources have made the first principle calculations more popular than ever as they have become more robust and stable. That is why in this work we have studied different topics using this same approach.

In chapter 2, we studied the battery systems comparing various electrolyte additives yielding different passionating layers on the metal electrode. The motivation behind this comparison was to improve on the surface properties of the electrode-electrolyte interface in order to mitigate dendritic growth. This type of high throughput material search is one of the main strengths of computational chemistry. We also developed a macroscopic model that helps us understand the initial nucleation of irregularities on a perfectly flat surface. This model is generic enough that it is capable of enlightening not only electro-deposition processes but also electro-polishing as one is the time reversal of the other. A natural progression of this work would be testing the model in different contexts.

In chapter 3, we worked on superconductor technologies, investigating the manufacturing recipe of Nb_3Sn for further improvement. This material is a very promising candidate to replace the use of pure niobium in radio frequency accelerators. Having a higher theoretical limit for quality factor, it should make it possible to cut down energy losses in the operation of the accelerators signifi-

cantly. We explored the microscopic mechanisms by which niobium mixes with tin to form Nb_3Sn. To overcome practical limitations, a better understanding of these mechanisms can be very useful.

Once discovered, the transformation mechanism from BCC lattice to A15 could shed light on the root cause of the defects observed in Nb_3Sn coatings. We presented two pathways that connect the two structures and ran a nudged elastic band to determine the energy barrier. Despite the low energy of the transformation, we failed to construct a stable BCC-A15 interface in a common planar lattice. Further investigation could provide a better lattice match which will then enable the study of interface dynamics.

Chapter 4 covers the first attempt to run molecular dynamics using JDFT. Theoretically, as shown in this thesis, JDFT dynamics should give the same rare event rates as full *ab initio* MD. We put this idea under inspection and studied the diffusion of hydroxyl ion in water. We overcame the practical issues like the droplets dissolving into JDFT fluid in a very simple and intuitive manner, but this may not be the best strategy. To a great extent, we reproduced the time scale of the proton hopping (Grotthuss mechanism) by which OH^- moves in water. In order to prove JDFT dynamics robust and accurate, demonstrations with longer simulations are vital. Other forms of fluid approximations, especially less empirical methods like classical density functional theoretical models should also be utilized to test JDFT dynamics. The droplet size remains a limiting factor on how long a simulation can run. The procedure can benefit from a more sophisticated time integration algorithm which deals with the mixing differently, allowing the simulation to run for longer times.

Chapter 4 is the first attempt to run molecular dynamics using JDFT. Theo-

retically, as shown in this thesis, JDFT dynamics gives the same rare event rates as full *ab initio* MD. We put this idea under inspection and studied the diffusion of hydroxyl ion in water. To a great extent, we reproduced the time scale of the proton hopping (Grotthuss mechanism) by which OH^- moves in water.

In order to prove JDFT dynamics robust and accurate, demonstrations with longer simulations are vital. Other forms of fluid approximations, especially less empirical methods like classical density functional theoretical models should also be utilized to test JDFT dynamics. We overcame the practical issues like the droplets dissolving into JDFT fluid in a very simple and intuitive manner. But this may not be the best strategy. The droplet size remains a limiting factor on how long a simulation can run. The procedure can benefit from a more sophisticated time integration algorithm which deals with the mixing differently while allowing the simulation to run for longer times.

JDFTx is a great open source tool for quantum chemistry applications [89]. It is the first implementation of JDFT, and it has unique features when it comes to solvated systems. It was also one of the first tools that implemented GPU support to accelerate the calculations. Despite having all these advantages, the community behind it is somewhat limited. For better testing, bug fixes and feature implementation a larger group of contributors is essential. In order to grow the user base, it is crucial to integrate it better with umbrella tools like ASE [7] and Materials project [41]. pythonJDFTx [70] is a good starting point in this direction but it is only a first step. Greater outreach to the computational physics community, introducing the advantages of JDFTx over legacy tools and familiarizing physicists with it, would help significantly. With a growing community behind it, JDFTx will be able to continue its growth and reach its full potential.

BIBLIOGRAPHY

[1] http://www.physics.rutgers.edu/~dhv/uspp/. 12

[2] Noam Agmon. The grotthuss mechanism. *Chemical Physics Letters*, 244(5):456–462, 1995. 49

[3] O. Andreussi, I. Dabo, and N. Marzari. *J. Chem. Phys*, 136:064102, 2012. 15, 16

[4] T. A. Arias, M. C. Payne, and J. D. Joannopoulos. *Phys. Rev. Lett*, 69(7):1077, 1992. 12

[5] Michiaki Arita, David R Bowler, and Tsuyoshi Miyazaki. Stable and efficient linear scaling first-principles molecular dynamics for 10000+ atoms. *Journal of Chemical Theory and Computation*, 10(12):5419–5425, 2014. 43

[6] Doron Aurbach, Yair Ein-Eli, Orit Chusid, Yaakov Carmeli, Matsliach Babai, and Herzel Yamin. The correlation between the surface chemistry and the performance of li-carbon intercalation anodes for rechargeable rocking-chairtype batteries. *Journal of The Electrochemical Society*, 141(3):603–611, 1994. 12

[7] S. R. Bahn and K. W. Jacobsen. An object-oriented scripting interface to a legacy electronic structure code. *Comput. Sci. Eng.*, 4(3):56–66, MAY-JUN 2002. 33, 61

[8] Perla B Balbuena and Yixuan Wang. *Lithium-ion batteries: solid-electrolyte interphase*. Imperial college press London, 2004. 12

[9] Chaoyue Becker, Sam Posen, Nickolas Groll, Russell Cook, Christian M. Schleptz, Daniel Leslie Hall, Matthias Liepe, Michael Pellin, John Za-

sadzinski, and Thomas Proslier. Analysis of nb3sn surface layers for superconducting radio frequency cavity applications. *Applied Physics Letters*, 106(8), 2015. 32

[10] Rémy Besson, Sylvain Guyot, and Alexandre Legris. Atomic-scale study of diffusion in a15 nb_3Sn. *Phys. Rev. B*, 75:054105, Feb 2007. 32

[11] M. Born and R. Oppenheimer. Zur quantentheorie der molekeln. *Annalen der Physik*, 389(20):457–484, 1927. 2

[12] DR Bowler and T Miyazaki. methods in electronic structure calculations. *Reports on Progress in Physics*, 75(3):036503, 2012. 43

[13] R. Car and M. Parrinello. Unified approach for molecular dynamics and density-functional theory. *Phys. Rev. Lett.*, 55:2471–2474, Nov 1985. 42

[14] Gerbrand Ceder, Geoffroy Hautier, Anubhav Jain, and Shyue Ping Ong. Recharging lithium battery research with first-principles methods. *Mrs Bulletin*, 36(03):185–191, 2011. 10

[15] J. N. Chazalvier. *Physical Review A*, 42(12), 1990. 11

[16] Yaron S. Cohen, Yair Cohen, and Doron Aurbach. Micromorphological studies of lithium electrodes in alkyl carbonate solutions using in situ atomic force microscopy. *The Journal of Physical Chemistry B*, 104(51):12282–12291, 2000. 11

[17] G.W. Cullen. Preparation and properties of niobium (columbium) stannide on insulating substrates. *Trans. AIME*, Vol: 230, Dec 1964. ix, 33

[18] CJT de Grotthuss. Sur la décomposition de leau et des corps quelle tient en dissolution à laide de lélectricité. *Galvanique. Ann. Chim*, 1806. 49

[19] Nicolas Dupre, Marine Cuisinier, and Dominique Guyomard. *The Electrochemical Society Interface*, pages 61–69, 2011. 10

[20] Henry Eyring. The activated complex in chemical reactions. *The Journal of Chemical Physics*, 3(2):107–115, 1935. 44

[21] Enrico Fermi. Statistical method to determine some properties of atoms. *Rend. Accad. Naz. Lincei*, 6:602–607, 1927. 5

[22] Richard A. Friesner. Ab initio quantum chemistry: Methodology and applications. *Proceedings of the National Academy of Sciences of the United States of America*, 102(19):6648–6653, 2005. 6

[23] Martin Fuchs and Matthias Scheffler. Ab initio pseudopotentials for electronic structure calculations of poly-atomic systems using density-functional theory. *Computer Physics Communications*, 119(1):67 – 98, 1999. 32

[24] P. Ganesh, P. R. C. Kent, and De en Jiang. *Journal of Physical Chemistry C*, 116:24476–24481, 2012. 11, 15

[25] P. Ganesh, Jeongnim Kim, Changwon Park, Mina Yoon, Fernando A. Reboredo, and Paul R. C. Kent. *J. Chem. Theory Comput.*, 10(53185323), 2014. 10, 15

[26] Kevin F. Garrity, Joseph W. Bennett, Karin M. Rabe, and David Vanderbilt. Pseudopotentials for high-throughput dft calculations. *Computational Materials Science*, 81(0):446 – 452, 2014. 12, 49

[27] John B. Goodenough. Rechargeable batteries: challenges old and new. *Journal of Solid State Electrochemistry*, 16(6):2019–2029, 2012. 10

[28] A Grassellino, A Romanenko, D Sergatskov, O Melnychuk, Y Trenikhina, A Crawford, A Rowe, M Wong, T Khabiboulline, and F Barkov. Nitrogen and argon doping of niobium for superconducting radio frequency cavities: a pathway to highly efficient accelerating structures. *Superconductor Science and Technology*, 26(10):102001, 2013. 31

[29] Deniz Gunceler and TA Arias. Universal iso-density polarizable continuum model for molecular solvents. 15, 16

[30] Deniz Gunceler, Kendra Letchworth-Weaver, Ravishankar Sundararaman, Kathleen A Schwarz, and T A Arias. The importance of nonlinear fluid response in joint density-functional theory studies of battery systems. *Modelling and Simulation in Materials Science and Engineering*, 21(7):074005, 2013. 10, 11, 12, 15, 16, 49

[31] Deniz Gunceler, Kathleen A Schwarz, Ravishankar Sundararaman, Kendra Letchworth-Weaver, and T A Arias. Nonlinear solvation models: Dendrite suppression on lithium surfaces. In *16th International Workshop on Computation Physics and Materials Science: Total Energy and Force Methods*, 2013. 10, 11, 12, 26, 29

[32] Jean-Pierre Hansen and Ian R McDonald. *Theory of simple liquids*. Elsevier, 1990. 7

[33] Katherine J. Harry, Daniel T. Hallinan, Dilworth Y. Parkinson, Alastair A. MacDowell, and Nitash P. Balsara. *Nature Materials*, 13:6973, 2014. 11

[34] Graeme Henkelman and Hannes Jónsson. A dimer method for finding saddle points on high dimensional potential surfaces using only first derivatives. *The Journal of chemical physics*, 111(15):7010–7022, 1999. 45

[35] Jonathan D. Herr and Ryan P. Steele. Accelerating ab initio molecular dynamics simulations by linear prediction methods. *Chemical Physics Letters*, 661:42 – 47, 2016. 43

[36] B. Hillenbrand and H. Martens. Superconducting nb3sn cavities with high quality factors and high critical flux densities. *Journal of Applied Physics*, 47(9), 1976. 31

[37] B. Hillenbrand, H. Martens, H. Pfister, K. Schnitzke, and Y. Uzel. Superconducting nb3sn cavities with high microwave qualities. *IEEE Transactions on Magnetics*, 13(1):491–495, Jan 1977. 31

[38] Khang Hoang. *Phys. Rev. Applied*, 3:024013, Feb 2015. 10, 15

[39] P. Hohenberg and W. Kohn. Inhomogeneous electron gas. *Physical Review*, 136(3B):B864–B871, nov 1964. 6

[40] Markus Jäckle and Axel Groß. Microscopic properties of lithium, sodium, and magnesium battery anode materials related to possible dendrite growth. *The Journal of Chemical Physics*, 141(17), 2014. x, 10, 11, 12, 25

[41] Anubhav Jain, Shyue Ping Ong, Geoffroy Hautier, Wei Chen, William Davidson Richards, Stephen Dacek, Shreyas Cholia, Dan Gunter, David Skinner, Gerbrand Ceder, and Kristin a. Persson. The Materials Project: A materials genome approach to accelerating materials innovation. *APL Materials*, 1(1):011002, 2013. 10, 61

[42] Maarten De Jong, Wei Chen, Thomas Angsten, Anubhav Jain, Randy Notestine, Anthony Gamst, Marcel Sluiter, Chaitanya Krishna Ande, Sybrand Van Der Zwaag, Jose J Plata, and et al. Charting the com-

plete elastic properties of inorganic crystalline compounds. *Scientific Data*, 2:150009, 2015. ix, 33

[43] HANNES JNSSON, GREG MILLS, and KARSTEN W. JACOBSEN. *Nudged elastic band method for finding minimum energy paths of transitions*, pages 385–404. 33

[44] S. C. L. Kamerlin, M. Haranczyk, and A. Warshel. *J. Phys. Chem. B*, 113:1253, 2009. 15

[45] Kiyoshi Kanamura, Soshi Shiraishi, and Zenichiro Takehara. *Journal of the Electrochemical Society*, 143(7):2187–2197, 1996. 12, 26, 29

[46] Kisuk Kang, Ying Shirley Meng, Julien Bréger, Clare P Grey, and Gerbrand Ceder. Electrodes with high power and high capacity for rechargeable lithium batteries. *Science*, 311(5763):977–980, 2006. 10

[47] VG Karpov, YA Kryukov, IV Karpov, and M Mitra. Field-induced nucleation in phase change memory. *Physical Review B*, 78(5):052201, 2008. 18

[48] VG Karpov, REE Maltby, IV Karpov, and E Yalon. Field-induced nucleation in the presence of a metal electrode. *Physical Review Applied*, 3(4):044004, 2015. 18

[49] P. Kneisel, G. Ciovati, P. Dhakal, K. Saito, W. Singer, X. Singer, and G.R. Myneni. Review of ingot niobium as a material for superconducting radiofrequency accelerating cavities. *Nuclear Instruments and Methods in Physics Research Section A: Accelerators, Spectrometers, Detectors and Associated Equipment*, 774:133 – 150, 2015. 31

[50] P. Kneisel, O. Stoltz, and J. Halbritter. Measurements of superconducting

nb3sn cavities in the ghz range. *IEEE Transactions on Magnetics*, 15(1):21–24, Jan 1979. 31

[51] Shinichi Komaba, Toru Ishikawa, Naoaki Yabuuchi, Wataru Murata, Atsushi Ito, and Yasuhiko Ohsawa. *Applied Materials & Interfaces*, 3:41654168, 2011. 12, 26, 29

[52] Ch. E. Lekka, M. J. Mehl, N. Bernstein, and D. A. Papaconstantopoulos. Tight-binding simulations of nb surfaces and surface defects. *Phys. Rev. B*, 68:035422, Jul 2003. 36

[53] Kendra Letchworth-Weaver and TA Arias. Joint density functional theory of the electrode-electrolyte interface: Application to fixed electrode potentials, interfacial capacitances, and potentials of zero charge. *Physical Review B*, 86(7):075140, 2012. 8

[54] Kevin Leung and Joanne L. Budzien. Ab initio molecular dynamics simulations of the initial stages of solid-electrolyte interphase formation on lithium ion battery graphitic anodes. *Phys. Chem. Chem. Phys.*, 12:6583–6586, 2010. 10, 15

[55] Mel Levy. Universal variational functionals of electron densities, first-order density matrices, and natural spin-orbitals and solution of the v-representability problem. *Proc Natl Acad Sci U S A*, 76(12):6062–6065, Dec 1979. 16592733[pmid]. 6

[56] Elliott H Lieb. Density functionals for coulomb systems. *International Journal of Quantum Chemistry*, 24(3):243–277, 1983. 6

[57] Elliott H. Lieb and Barry Simon. Thomas-fermi theory revisited. *Phys. Rev. Lett.*, 31:681–683, Sep 1973. 5

[58] Yingying Lu, Zhengyuan Tu, and Lynden A. Archer. Stable lithium electrodeposition in liquid and nanoporous solid electrolytes. *Nature Materials*, 13:961969, 2014. 11, 12, 24, 26, 27, 29

[59] Yingying Lu, Zhengyuan Tu, Jonathan Shu, and Lynden A. Archer. Stable lithium electrodeposition in salt-reinforced electrolytes. *Journal of Power Sources*, 279(0):413 – 418, 2015. 9th International Conference on Lead-Acid Batteries {LABAT} 2014. 12, 29

[60] Yingying Lu, Shaomao Xu, Jonathan Shu, Wajdi Issam A. Aladat, and Lynden A. Archer. High voltage {LIB} cathodes enabled by salt-reinforced liquid electrolytes. *Electrochemistry Communications*, 51(0):23 – 26, 2015. 12, 29

[61] Dominik Marx and Jurg Hutter. Ab initio molecular dynamics: Theory and implementation. *Modern methods and algorithms of quantum chemistry*, 1(301-449):141, 2000. 42

[62] B. T. Matthias, T. H. Geballe, S. Geller, and E. Corenzwit. Superconductivity of nb_3sn. *Phys. Rev.*, 95:1435–1435, Sep 1954. 31

[63] Matthew Z. Mayers, Jakub W. Kaminski, and Thomas F. Miller. *The Journal of Physical Chemistry C*, 116(50):26214–26221, 2012. 11

[64] Ryo Mogi, Minoru Inaba, Soon-Ki Jeong, Yasutoshi Iriyama, Takeshi Abe, and Zempachi Ogumi. *Journal of The Electrochemical Society*, 149(12):A1578–A1583, 2002. 12, 26, 29

[65] Stephan Mohr, Laura E Ratcliff, Luigi Genovese, Damien Caliste, Paul Boulanger, Stefan Goedecker, and Thierry Deutsch. Accurate and effi-

cient linear scaling dft calculations with universal applicability. *Physical Chemistry Chemical Physics*, 17(47):31360–31370, 2015. 43

[66] K. Momma and F. Izumi. *J. Appl. Crystallogr.*, 44:12721276, 2011. x, 14

[67] Motoaki Nishijima, Takuya Ootani, Yuichi Kamimura, Toshitsugu Sueki, Shogo Esaki, Shunsuke Murai, Koji Fujita, Katsuhisa Tanaka, Koji Ohira, Yukinori Koyama, et al. Accelerated discovery of cathode materials with prolonged cycle life for lithium-ion battery. *Nature communications*, 5, 2014. 10

[68] Kei Nishikawa, Takeshi Mori, Tetsuo Nishida, Yasuhiro Fukunaka, Michel Rossoa, and Takayuki Homma. *J. Electrochem. Soc.*, 157(11), 2010. 10

[69] Shyue Ping Ong, Vincent L Chevrier, Geoffroy Hautier, Anubhav Jain, Charles Moore, Sangtae Kim, Xiaohua Ma, and Gerbrand Ceder. Voltage, stability and diffusion barrier differences between sodium-ion and lithium-ion intercalation materials. *Energy & Environmental Science*, 4(9):3680–3688, 2011. 10

[70] Yalcin Ozhabes. pythonjdftx. `https://github.com/yalcinozhabes/pythonJDFTx`, 2012. 33, 61

[71] Hasan S. Padamsee. Superconducting radio-frequency cavities. *Annual Review of Nuclear and Particle Science*, 64(1):175–196, 2014. 31

[72] I. Papadimitriou, C. Utton, and P. Tsakiropoulos. Ab initio investigation of the intermetallics in the nbsn binary system. *Acta Materialia*, 86:23 – 33, 2015. 32

[73] Min Sik Park, Sang Bok Ma, Dong Joon Lee, Dongmin Im, Seok-Gwang Doo, and Osamu Yamamoto. *Scientific Reports*, 4(3815), 2014. 10, 16

[74] E. Peled. *Journal of the Electrochemical Society*, 126:2047–2051, 1979. 10

[75] J. P. Perdew, K. Burke, and M. Ernzerhof. *Phys. Rev. Lett.*, 77:3865, 1996. 12, 32, 49

[76] Kristin Persson, Yoyo Hinuma, Ying Shirley Meng, Anton Van der Ven, and Gerbrand Ceder. *Phys. Rev. B*, 82(125416), 2010. 10, 15

[77] Kristin Persson, Vijay A. Sethuraman, Laurence J. Hardwick, Yoyo Hinuma, Ying Shirley Meng, Anton van der Ven, Venkat Srinivasan, Robert Kostecki, and Gerbrand Ceder. *J. Phys. Chem. Lett*, 1:11761180, 2010. 10, 15

[78] SA Petrosyan, Jean-Francois Briere, David Roundy, and TA Arias. Joint density-functional theory for electronic structure of solvated systems. *Physical Review B*, 75(20):205105, 2007. 8

[79] Matthew B. Pinsona and Martin Z. Bazant. *Journal of The Electrochemical Society*, 160(2):A243–A250, 2013. 11

[80] Sam Posen and Matthias Liepe. Advances in development of nb_3Sn superconducting radio-frequency cavities. *Phys. Rev. ST Accel. Beams*, 17:112001, Nov 2014. 31

[81] Wolfgang Quapp, Michael Hirsch, Olaf Imig, and Dietmar Heidrich. Searching for saddle points of potential energy surfaces by following a reduced gradient. *Journal of computational chemistry*, 19(9):1087–1100, 1998. 45

[82] Venkatasailanathan Ramadesigana, Paul W. C. Northropa, Sumitava Dea, Shriram Santhanagopalanb, Richard D. Braatzc, and Venkat R. Subramaniana. *J. Electrochem. Soc.*, 159(3):R31–R45, 2012. 11

[83] SVEND ERIK RASMUSSEN. Preparation of single phases and single crystals of niobiumgermanium compounds. *ACTA CHEMICA SCANDINAVICA SERIES A-PHYSICAL AND INORGANIC CHEMISTRY*, 31(2):79–82, 1977. ix, 33

[84] Sebastian Schnur and Axel Groß. Challenges in the first-principles description of reactions in electrocatalysis. *Catalysis Today*, 165(1):129 – 137, 2011. 15

[85] Siqi Shi, Peng Lu, Zhongyi Liu, Yue Qi, Louis G. Hector Jr., Hong Li, and Stephen J. Harris. *Journal of Physical Chemistry C*, 114:2090320906, 2010. 10, 11

[86] Siqi Shi, Peng Lu, Zhongyi Liu, Yue Qi, Louis G. Hector Jr., Hong Li, and Stephen J. Harris. *Journal of American Chemical Society*, 134:1547615487, 2012. 10, 11

[87] Siqi Shi, Yue Qi, Hong Li, and Louis G. Hector Jr. *Journal of Physical Chemistry C*, 117:85798593, 2013. 10, 11

[88] Soshi Shiraishi, Kiyoshi Kanamura, and Zenichiro Takehara. *J. Appl. Electrochem.*, 29:869–881, 1999. 10

[89] R. Sundararaman, D. Gunceler, K. Letchworth-Weaver, and T.A. Arias. JDFTx. `http://jdftx.sourceforge.net`, 2012. 12, 32, 49, 61

[90] Ravishankar Sundararaman and T. A. Arias. *Phys. Rev. B*, 87:165122, 2013. 13

[91] Vernica M. Snchez, Mariela Sued, and Damin A. Scherlis. First-principles molecular dynamics simulations at solid-liquid interfaces with a continuum solvent. *The Journal of Chemical Physics*, 131(17), 2009. 15

[92] Ken Tasaki. *J. Phys. Chem. C*, 118(14431450), 2014. 10, 15

[93] J. THEWLIS and A. R. DAVEY. Thermal expansion of grey tin. *Nature*, 174(4439):1011–1011, Nov 1954. ix, 33

[94] Sascha Thinius, Mazharul M. Islam, Paul Heitjans, and Thomas Bredow. *J. Phys. Chem. C*, 118(22732280), 2014. 10, 15

[95] L. H. Thomas. The calculation of atomic fields. *Mathematical Proceedings of the Cambridge Philosophical Society*, 23(5):542548, Jan 1927. 5

[96] Mukul D. Tikekar, Lynden A. Archer, and Donald L. Koch. *J. Electrochem. Soc.*, 161(6), 2014. 11, 12

[97] N. Troullier and José Luís Martins. Efficient pseudopotentials for plane-wave calculations. *Phys. Rev. B*, 43:1993–2006, Jan 1991. 32

[98] Donald G Truhlar, William L Hase, and James T Hynes. Current status of transition-state theory. *The Journal of Physical Chemistry*, 87(15):2664–2682, 1983. 44

[99] Mark Tuckerman, Kari Laasonen, Michiel Sprik, and Michele Parrinello. Ab initio molecular dynamics simulation of the solvation and transport of h3o+ and oh-ions in water. *The Journal of Physical Chemistry*, 99(16):5749–5752, 1995. 52

[100] Mark E Tuckerman, Amalendu Chandra, and Dominik Marx. Structure and dynamics of oh-(aq). *Accounts of chemical research*, 39(2):151–158, 2006. 52

[101] A. T. van Kessel, H. W. Myron, and F. M. Mueller. Electronic structure of nb_3sn. *Phys. Rev. Lett.*, 41:181–184, Jul 1978. 32

[102] David Vanderbilt. Soft self-consistent pseudopotentials in a generalized eigenvalue formalism. *Phys. Rev. B*, 41:7892–7895, Apr 1990. 12, 49

[103] Loup Verlet. Computer "experiments" on classical fluids. i. thermodynamical properties of lennard-jones molecules. *Phys. Rev.*, 159:98–103, Jul 1967. 49

[104] Penghao Xiao, Daniel Sheppard, Jutta Rogal, and Graeme Henkelman. Solid-state dimer method for calculating solid-solid phase transitions. *The Journal of Chemical Physics*, 140(17), 2014. 35

[105] Kang Xu. Nonaqueous liquid electrolytes for lithium-based rechargeable batteries. *Chemical Reviews*, 104(10):4303–4418, 2004. 12

[106] Guangyuan Zheng, Seok Woo Lee, Zheng Liang, Hyun-Wook Lee, Kai Yan, Hongbin Yao, Haotian Wang, Weiyang Li, Steven Chu, and Yi Cui. Interconnected hollow carbon nanospheres for stable lithium metal anodes. *Nature Nanotechnology*, 9:618623, 2014. 10, 11